Spring 2022

Growth, Characterization and Evaluation of CdZnTeSe Single Crystals for Room Temperature Radiation Detectors

Ritwik Nag

GROWTH, CHARACTERIZATION AND EVALUATION OF CDZNTESE SINGLE CRYSTALS FOR ROOM TEMPERATURE RADIATION DETECTORS

by

Ritwik Nag

Bachelor of Science
University of Calcutta, India, 2020

Submitted in Partial Fulfillment of the Requirements

For the Degree of Master of Science in

Electrical Engineering

College of Engineering and Computing

University of South Carolina

2022

Accepted by:

Krishna C. Mandal, Director of Thesis

Guoan Wang, Reader

Tracey L. Weldon, Interim Vice Provost and Dean of the Graduate School

DEDICATION

I would like to dedicate this work to my parents.

ACKNOWLEDGEMENTS

First and foremost, I am deeply grateful to my advising supervisor Prof. Krishna C. Mandal for his invaluable guidance, continuous support, and encouragement without which this work would not have been possible. I would like to express my heartfelt gratitude to him for unrestricted use of his research laboratories. His scientific excitement inspires me, and I am glad that I had this opportunity to work him.

I am thankful to Dr. Sandeep K. Chaudhuri for his technical guidance, training, and critical insights I needed to complete the research work, especially his support in crystal growth, characterization, and radiation detection measurements. I would also like to thank Joshua W. Kleppinger and OmerFaruk Karadavut for taking time to train me, sharing knowledge, and helping me in device fabrication, characterizations, and evaluations.

I would like to thank my MS thesis committee member Prof. Guoan Wang for taking time to oversee my research, as well as encourage and support my work.

I also like to thank Electron Microscopy Centre for SEM-EDX studies, Chemistry and Biochemistry Dept. for XRD, and Dr. Stavros G. Karakalos for XPS measurements.

I thank Ms. Jenny Balestrero, Ms. Meredith Higgs, and Mr. Brian Hull for their administrative and technical assistance throughout my graduate studies at UofSC.

Finally, I would like to thank my parents and my family members for encouraging me and tirelessly supporting me in this journey.

ABSTRACT

In this research work $Cd_{0.9}Zn_{0.1}Te_{0.03}Se_{0.97}$ (CZTS) single crystals were grown using in-house zone refined 7N (99.99999%) purity elements through vertical Bridgman (VBM) method and vertical gradient freeze (VGF) method. The morphological, compositional, and structural characteristics were then performed on the grown CZTS crystals. The x-ray diffraction (XRD) analysis on the grown crystals showed sharp diffraction peaks indicating a highly crystalline nature, with a lattice constant of ~6.45 Å. The elemental and stoichiometric ratio of the grown CZTS crystals were examined by using energy-dispersive x-ray analysis (EDX), which confirmed the formation of the quaternary compound in its desired stoichiometry. Scanning electron microscopy (SEM) on the surface of the processed (etched and polished) crystals displayed a smooth surface with no noticeable defects or cracks. The oxidation states of the precursor elements were analyzed using x-ray photoelectric spectroscopy (XPS), which was found to be relevant to the states found in the precursor compounds such as $Cd_{0.9}Zn_{0.1}Te$ (CZT) and CdTe. Current-voltage characterizations were performed on the fabricated devices with 11 × 11 × 3 mm^3 dimension wafer cut out from the grown ingots. The leakage current was low for crystals grown using the vertical Bridgman method (VBM) as well as for the vertical gradient freeze method (VGF). The bulk resistivity was in the range of 10^9 to 10^{10} Ω-cm and the log J – log V plots revealed a trap space charge limited current (SCLC) mechanism at moderate bias. Alpha spectroscopy using ^{241}Am (americium radio isotope as a radiation source) was

carried out to calculate the charge transport properties in the fabricated devices. The mobility-lifetime product was found to be ~1.5×10^{-3} cm^2/V while the drift mobility was calculated to be ~710 cm^2/V-s. The observed electron-transport properties were in good agreement with the reported values for the best CZTS crystals. The single pass Bridgman technique and the vertical gradient technique, used to grow the crystals can help reduce the crystal growth duration and the production cost related to large volume growth of CZTS semiconductor crystal boules, without diminishing any of the charge transport and radiation detection properties found in CZTS crystals.

TABLE OF CONTENTS

LIST OF TABLES

LIST OF FIGURES

LIST OF SYMBOLS

eV	Electron Volt (energy unit)
K	Kelvin scale (temperature unit)
Ω	Ohm (resistance unit)
τ	Charge carrier lifetime
μ	Mobility
V	Voltage
I	Current
Å	Angstrom (length unit)
λ	Wavelength
a	Lattice constant of a crystal
E_k	Kinetic Energy
Φ	Work function
E_B	Binding energy
ρ	Resistivity

μCi	Micro Curie (radiation unit)
d	Spacing/thickness
E	Electric field
v_d	Drift velocity under an electric field

LIST OF ABBREVIATIONS

Br2MeOH ..... Bromine-methanol solution

CCE..... Charge collection efficiency

Cd..... Cadmium (element)

CdTe..... Cadmium telluride

CMP .....Chemo-mechanical polishing

CT .....Computed tomography

CZT/CdZnTe..... Cadmium-zinc-telluride

CZTS/CdZnTeSe .....Cadmium zinc telluride selenide

EDX ..... Energy dispersive x-ray spectroscopy

FWHM .....Full width half maxima

GDMS ..... Glow discharge mass spectroscopy

HPGe.....High purity germanium

ID ..... Inner diameter

In .....Indium (element)

MCA .....Multichannel analyzer

OD..... Outer diameter

PCB.....Printed circuit board

PHS ..... Pulse height spectrum

ppb..... Parts per billion

ppm .....Parts per million

PWM ..... Pulse-width modulated

RT ..... Room temperature

SCLC ..... Space charge limited current

Se ..... Selenium (element)

Si ..... Silicon (element)

Te ..... Tellurium (element)

THM ..... Travelling heater method

TOF ..... Time-of-flight

TSA ..... Transportation Security Administration

VBM ..... Vertical Bridgman method

VGF ..... Vertical gradient freeze

XPS ..... X-ray photoelectron spectroscopy

XRD ..... X-ray diffraction

Z ..... Atomic number

ZR ..... Zone refined

CHAPTER 1

GENERAL INTRODUCTION

1.1 INTRODUCTION

Identification, accounting and monitoring of penetrating nuclear radiations such as x-rays and gamma-rays are important components for a wide variety of applications such as security screening at the port of entries, control and accounting of nuclear fuel processing at nuclear power facilities, safeguarding of stored spent nuclear fuels casks, studying nuclear interactions with matter in deep space for understanding cosmic events and planetary atmosphere, and accounting of radiations for medical imaging using x-ray radiography, mammography, computed tomography (CT). Nuclear spectroscopy for above applications, uses a *radiation detector* attached to a spectrometer followed by a peak detection algorithm to identify the radioisotopes from the detected peak energies. In *solid-state* radiation detector, semiconductor crystal with some unique properties (as opposed to gases) is used as a detecting material, which absorb ionizing radiation such as x-rays and gamma-rays from the radioactive materials and generate electrical charge carriers that produces electrical signals under an applied voltage. The electrical signals, known as *pulses*, provide a measure of the identity, energy, and counts of incident radiations.

The goal of this thesis work was to develop CdZnTeSe (CZTS) quaternary semiconductor based *solid-state direct-readout* radiation detector and to demonstrate its application in alpha particle detection at room temperature. "Direct-readout" means direct

conversion of incident radiation into electrical signal without a need of any secondary photoconversion system. The work performed under this goal is divided into three major research objectives. First is to grow CZTS single crystal semiconductor using two growth techniques – (i) modified vertical Bridgman method and (ii) vertical gradient freeze technique. Second objective is to perform optical and electrical characterization on the grown CZTS crystal to measure for required nuclear detection properties. The third objective is to fabricate a nuclear radiation device on the characterized CZTS crystal and evaluate its radiation detection capabilities using pulse height spectroscopy with alpha particle radiation source.

1.2 THESIS OVERVIEW

The thesis is divided into five chapters. Chapter 1: General Introduction provides background and significance of radiation detectors, especially semiconductor based solid-state detector, a brief discussion on advantages and disadvantages of currently used semiconductors for radiation detectors, a review of the properties of CZTS compared to ideal semiconductors for radiation detection, and the novelty of the research work.

Chapter 2 focuses on the crystal growth methods of CZTS crystals using a modified vertical Bridgman technique and vertical gradient freeze technique. CZTS crystals were grown from high purity elemental precursor materials with indium (In) dopant and excess tellurium (Te) as solvent. An overview of Bridgman growth technique and gradient freeze technique, CZTS crystal growth process along with temperature profile of growth furnace during crystal growth, and subsequent crystal processing is discussed in this chapter. Finally, the device fabrication process on grown CZTS crystals is described.

Chapter 3 describes the various characterization techniques performed on the grown quaternary CZTS crystals. The characterization comprises of identification of the various compositional, stoichiometric, optical, and electrical characteristics of CZTS semiconductor. For example, scanning electron microscopy (SEM) was carried out for morphological characterization and detection of any surface defects. X-ray photoelectron spectroscopy (XPS) and energy dispersive x-ray spectroscopy (EDX) were carried out to determine stoichiometric and compositional characteristics, and x-ray diffraction (XRD) was carried out to determine structural characteristics of CZTS crystal lattice. Finally, current-voltage (I-V) measurements were performed to determine electrical characteristics such as resistivity and Ohmic and Schottky behavior of semiconductor-metal junction.

Chapter 4 describes the radiation detection studies on the fabricated device. Pulse height spectroscopy using americium (^{241}Am) as radiation source for alpha particles, was performed to evaluate if the fabricated CZTS detector could detect incident alpha particles with high resolution. The radiation detection measurements were then used to study the charge transport properties within the CZTS device structure. The charge collection efficiency (CCE), the drift mobility, and the mobility lifetime product were calculated from the alpha spectroscopy studies. The resolution was calculated from the full width half maxima (FWHM) of the pulse signal generated by the incident alpha particles.

Chapter 5: Conclusion summarizes key results or findings of the entire work related to the research goal of developing CZTS based nuclear detector, dissemination of results, and suggests further research needs to be carried out.

1.3 CURRENTLY AVAILABLE RADIATION DETECTORS

The most common radiation detector used to be the gas proportional counter or Geiger-Muller counter which uses a gas-filled tube with a central wire at high voltage to collect the ionization produced by incident radiation. These radiation detectors are relatively cheap and can be made rugged, however they cannot distinguish between alpha, beta, and gamma radiation and suffer from timing speed limitations [1]. Scintillator based radiation detectors such as NaI(TI) give off light (instead of electrical charges) when radiation interacts with them. A secondary system, commonly a photomultiplier tube (PMT) or avalanche photodiodes (APD) optical detector is used to detect the light produced by radiation and then to convert it to electrical pulses with readout electronics. NaI scintillator-based detection systems are often used for Transportation Security Administration (TSA) screening at the airport [2]. Response speeds can be quite fast with some scintillators, but main drawbacks are low energy resolution due to poor temperature stability and strong background noise [2-3].

Over past decades, semiconductor based solid-state "direct read-out" detectors have been proven to be more versatile radiation detectors that can accurately identify the type, state, and amount of nuclear radiation with high sensitivity and high resolution. In semiconductors, incident radiations generate charge carriers (instead of light) which can be collected under a given voltage to produce electric signal *directly* without any secondary system. Furthermore, in semiconductor material, only a few eV (energy) is necessary to create an electron-hole pair compared to 50 eV or more of energy in scintillator material. Thus, a much greater signal is generated in semiconductor detector than in scintillator for a given amount of energy deposited by a nuclear radiation [4]. Over the years different

semiconductor materials have been studied for gamma radiation detectors such as crystalline silicon (Si), high-purity germanium (HP Ge), mercuric iodide (HgI_2), and cadmium telluride (CdTe), cadmium zinc telluride (CZT), and aluminum indium phosphide (AlInP) to name a few [1-12].

Presently, high-purity germanium (HP Ge) detectors offer the highest performance with energy resolution of 0.2% using a benchmark 662 keV gamma-ray. Germanium (Ge) has a high atomic number to stop x-rays and gamma-rays, can be produced in large volumes (> 10 cm^3), and are widely used in environmental radiation and trace element measurements. However, due to its low bandgap of 0.67 eV at 300 K, germanium detectors require cryogenic cooling (<110 K) to function properly [5]. This makes the system bulky and increases power consumption to the level where the field applications are complicated. Consequently, there has been an enormous effort to develop semiconductor detectors that are compact and operable at room temperature (RT). An ideal semiconductor detector material for direct readout gamma ray detection should have high Z and be in a solid state to have a high stopping power, should have a wide bandgap for room temperature applications and reduce unnecessary cryogenic cooling systems, and have good energy resolution. Properties of some semiconductor radiation detectors (commercially available and being developed) are compared to the ideal properties for room-temperature radiation detector in Table 1.1 [2, 4, 6, 8, 10-14].

Table 1.1 Properties of current semiconductors for direct readout radiation detectors

Semi-conductor	**Energy bandgap at 300 K E_g (eV)**	**Growth T_{MP} (°C)**	**Atomic number Z**	**Density (g/cm^3)**	**Electron-hole pair creation energy, W, (eV)**	**Resistivity (Ω-cm)**	**Mobility, μ (cm^2/Vs) hole/ electron**	**Carrier lifetime, τ ($\times 10^{-6}$sec)**	**Mobility-lifetime product of electron $\mu\tau_e$, (cm^2/V)**
Ideal	***1.6-2.1***	***700-1200***	***>50[a]***	**-**	***<3E_g***	***≥ 10^{10}***	**-**	**-**	***≥ 10^{-3}***
Ge	0.67	938	32	5.33	2.96	50	1900/3900	≥300	0.57
HgI_2	2.1	260	80, 53	6.4	~4.2	10^{12}	4/100	~2	10^{-4}
CdTe	1.5	950-1085	48, 52	6.2	4.43	10^{9}	100/1100	0.4	0.4×10^{-3}
CdZnTe (CZT)	1.6-1.9	1175	52	5.78	4.6	$>10^{10}$	120/1000	~1	10^{-3}
4H-SiC	3.27	1550-1750	14, 6	3.21	7.28	$>10^{12}$	115/1020	~1	0.8×10^{-3}

a: For detection of high energy x-ray and gamma ray

Compound semiconductors with compact form factor such as cadmium telluride (CdTe) and CdZnTe (CZT) have been the popular choice for room-temperature gamma-ray detector for the last couple of decades [6-10]. CZT and CdTe both are high-Z semiconductors meaning they have constituent elements with high atomic number (Z_{Cd} = 48, Z_{Zn} = 30, and Z_{Te} = 52) making these compound semiconductors very capable of stopping high-energy gamma-ray. Cadmium telluride (CdTe) with a bandgap of 1.5 eV at 300K offers good charge transport properties, however it generally exhibits a resistivity of ~10^8 – 10^9 Ω-cm, which is less than ideal for high resolution (low signal to noise ratio) gamma-ray detector [8]. Inclusion of Zn element in CdTe crystal lattice (i.e., CdZnTe or simply CZT) increases the bandgap energy to a range of 1.50 – 1.90 eV depending on Zn percentage in CZT stoichiometry, resulting in higher resistivity of 10^{11} Ω-cm [6, 9-10]. CZT demonstrated capability of room temperature operation and an energy resolution of

≤ 1% at 662 keV with up to 1.5 cm crystal length [10]. CZT, due to its wider band gap and high resistivity at room temperature, has become semiconductor of choice for radiation detectors in practical field applications such as homeland security, medical imaging, high-energy physics, space astronomy, and environmental monitoring [8, 10, 15-18]. However, CZT suffers from low crystal-growth yield, crystal defects such as sub-grain boundary, and poor hole transport.

CZT crystal are grown typically using vertical Bridgman growth (VBM) [7, 19] and travelling heater method (THM) [20-21]. Although large volume single crystals can be grown using these growth methods, the crystal growth yield is generally low – only about one-third of the grown ingot exhibits detector grade parameters for crystallinity, homogeneity, and resistivity. The low crystal-growth yield increases the manufacturing cost of CZT crystal, thereby increasing the cost of radiation spectrometers based on CZT detectors, and consequently inhibits wide-spread applications of CZT gamma-ray based imager or spectrometers. Crystal defect such as compositional nonuniformity due to Zn segregation, presence of Te inclusions, and high concentrations of sub-grain boundary networks limit the performance of CZT based detectors [6, 8, 15, 22]. The sub-grain boundary networks also cause compositional inhomogeneity which in turn reduces the crystal growth yield substantially leading to high cost of production and manufacturing [23-24]. The material defects can act as charge trapping centers, leading to the recombination (annihilation) of radiation induced charge carriers (electron and hole pairs) before they could contribute to output signal. This leads to poor charge transport properties such as low drift-velocity and shorter lifetime. CZT material also possesses much higher electron mobility (>1000 cm^2/Vs) compared to hole mobility (~120 cm^2/Vs) giving rise to

relative stationary hole movement within the electron collection time, resulting in incomplete charge collection.

1.4 INTRODUCTION TO CZTS SEMICONDUCTOR

Recent break-through studies [23-26] have shown that selenium (Se) inclusion in the CZT matrix can lead to reduction of the density of Te inclusions and formation of sub-grain boundaries. The resulting novel quaternary $Cd_{1-x}Zn_xTe_{1-y}Se_y$ material (hence forward CZTS) has the potential to be a better performing and cost-effective alternatives of CZT, the current leader in room temperature gamma-radiation detector applications. In addition, the formation of Cd vacancies is prohibited in CZTS as Se has the highest partial pressure among group VI elements [27]. CZTS grown by traveling heater method has demonstrated exceptionally high crystal growth yield (90%) with high axial and radial compositional homogeneity [23-24, 26-27].

Figure 1.1 shows the atomic arrangements of the constituents in a 64-atom CZTS (CdZnTeSe) primitive supercell. In this figure, Cd (pink spheres) are present at the corner of the cubic lattice and at the center of each face; Te (olive-green spheres) are present in the alternative tetrahedral void; Zn (grey spheres) are occupying some of Cd positions; and Se (lime-green sphere) occupying one of the Te positions. Selected physical and electrical properties of CZTS are listed in Table 1.2. With high-Z value for high stopping power for gamma ray, high bandgap (1.6 eV) offering room temperature operation, high-resistivity ($> 10^{10}$ Ω-cm) for high resolution, better homogeneity with lesser defects, and high crystal yield for lower production cost, the quaternary semiconductor CZTS has great potential to become the next state-of-the-art widely used room-temperature gamma-ray detectors. Roy et. al formerly at Brookhaven National Laboratory demonstrated a record high energy

resolution of 0.77% for 662 keV gamma rays on THM grown Frisch collar CZTS detectors [24]. Frisch collar detector is a unipolar detector design where output signal is due to only high-mobility electrons, thus compensating for low-mobility holes.

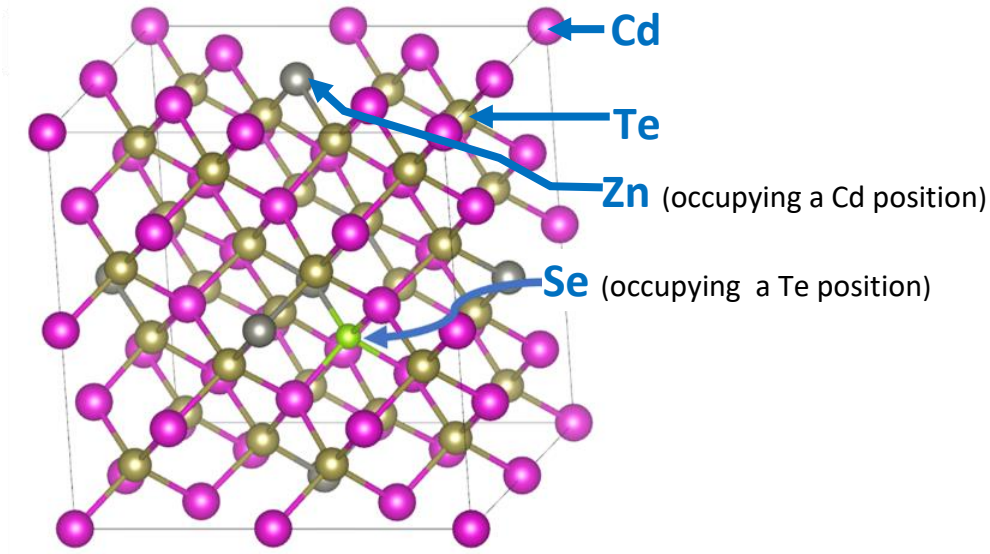

Figure 1.1 The zinc blende crystal lattice structure of $Cd_xZn_{1-x}Te_ySe_{1-y}$ showing positions of constituent elements.

Table 1.2 Physical and Structural Properties of CZTS at 300 K

Crystal Structure:	Zinc Blende
Lattice Constant	6.48 Å
Density; solid	5.8 g/cm^3
Band Gap:	1.6 eV @ 300K
Atomic Number:	Cd: 48, Zn: 30, Te: 52, Se: 34
Resistivity:	>10^{10} Ohm-cm
Electron Mobility:	>1000 cm^2/Vs
Hole Mobility:	~50 cm^2/Vs

1.5 NOVELTY OF PRESENT RESEARCH

The research effort was focused on growth of high-quality detector grade CZTS single crystal with desired properties for high performance gamma-ray detector at a lower manufacturing cost. To achieve this, CZTS compound was grown, for the first time, using two different growth methods - a modified vertical Bridgman method and vertical gradient freeze growth technique. The vertical Bridgman growth method reported here uses a single pass through the controlled heating zone in contrast to the previously reported multiple pass growth techniques, thus, reducing the growth duration by two third which would help to further reduce the cost of production of CZTS-based room-temperature detectors. Furthermore, in this thesis we report the growth of CZTS crystal by vertical gradient freeze (VGF) growth technique for the first time.

As detailed in the Chapter 2, typical Bridgman method involves crystal growth from a melt by progressively freezing the melt from one end to the other by moving the growth ampoule from high temperature (above melting point) to low temperature zone. Due to this motion of the ampoule, the growth interface can be affected by temperature fluctuations and thermal drift. To reduce temperature-related stress in growing crystal, the ampoule movement is kept very slow (1 4 mm/hr) making Bridgman growth process very time consuming. In VGF method, the heaters and the growth ampoule are stationary, hence it allows the heat transport to be controlled and stabilized.

The stoichiometric formula quaternary compound commonly referred to as CZTS is $Cd_{0.9}Zn_{0.1}Te_{1-y}Se_y$, with y being atomic ratio of selenium (Se) in the structure. The ratio of Se is an important factor for high-resolution gamma-ray detector properties of CZTS. We report here growth of CZTS single crystal with stoichiometry of $Cd_{0.9}Zn_{0.1}Te_{0.97}Se_{0.03}$

(CZTS) using in-house zone-refined 7 N (99.99999%) purity elemental precursors and characteristics of the grown compound required for room-temperature radiation detection. Furthermore, indium (In) dopant was used to further increase the resistivity of the grown CZTS crystal (higher the resistivity better the resolution) and to compensate for residual cadmium vacancies caused by excess tellurium.

CHAPTER 2

CRYSTAL GROWTH

2.1 OVERVIEW OF CRYSTAL GROWTH METHODS

Quaternary semiconductor CZTS crystals are reported to be grown using melt-growth techniques such as travelling heater method (THM) and Bridgman method in a sealed quartz ampoule [24, 27-29]. In melt-growth process, high purity constituent elements or compounds called precursors are thermally melted, then allowed to react enabling synthesis of desired compound, followed by controlled re-solidification to facilitate crystallization. The goal is to carry out synthesis of compound material in a homogeneous manner to achieve the targeted stoichiometry (atomic ratio). A seed crystal is used to perform the growth unidirectionally to achieve single crystallinity. Schematic diagrams of THM and Bridgman methods are presented in Figure 2.1 along with temperature profiles for CZTS crystal growth.

In the travelling heater method (THM), pre-synthesized polycrystalline compound is placed within a sealed quartz ampoule. A heater (furnace) travels along the length of the sealed ampoule creating a hot zone (solvent zone), where material to be grown is dissolved in a compatible solution. The solvent zone is migrated through the solid source material while maintaining a thermal gradient which ensures the accurate cooling rate for crystallization. Large volume detector grade single crystals can be obtained using THM. However, the rate of crystal growth is rather slow, typically 1-2 mm/day. In the Bridgman

growth method, single crystal is grown from a melt by progressively freezing the melt from one end to the other. The precursor material in quartz ampoule is first melted at a stationary hot zone which is kept at a temperature just above the melting point of the material to be grown. As the growth ampoule slowly travels from hot zone to a progressively cold zone through the furnace, the molten precursor gets solidified along with the seed crystal. The Bridgman growth process is faster (1-4 mm/hr) compared to THM, but often suffers from low crystal growth yield, presence of extended defects, and poor electron transport properties.

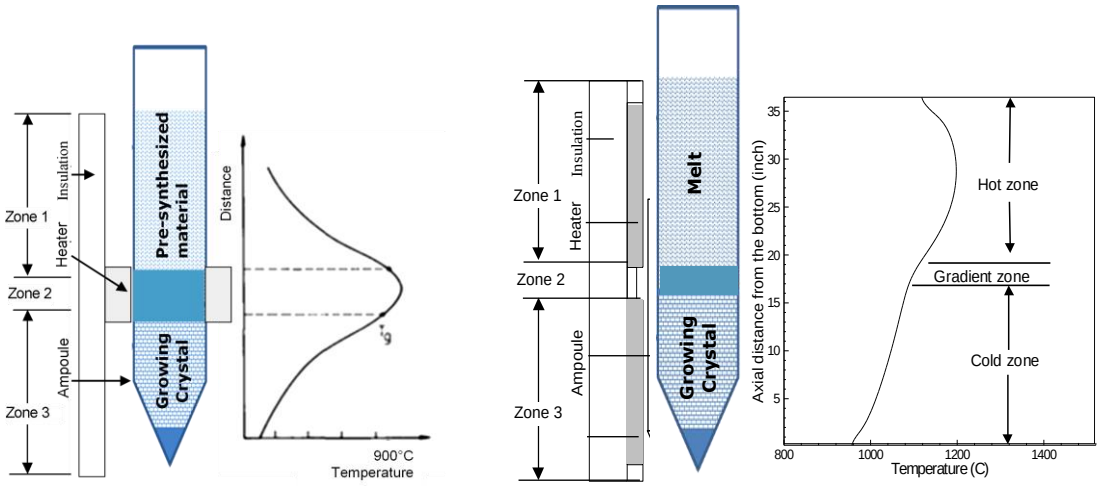

Figure 2.1 Schematic diagram and temperature profile of travelling heater method (left) and Bridgman method (right)

For the research presented here, two types of growth techniques were used to grow high-quality CZTS single crystals at a lower manufacturing cost: (i) single-pass modified vertical Bridgman method (VBM) and (ii) two-zone vertical gradient freeze (VGF) method. In the modified vertical Bridgman growth method, instead of multiple pass growth techniques our research group previously used [25, 28], a single pass through the controlled heating zone was used to reduce total crystal growth time by two third. Thus, this method

would greatly help in the reduction of production cost for CZTS material and thereby CZTS-based room-temperature radiation detectors. In addition, the VBM method used for the CZTS crystal growth was carried out at a growth temperature lower than that normally used in traveling heater methods used by other researchers mentioned above. This lessens temperature related stress on growing crystal and offers an opportunity to reduce crystal defects such as sub-grain boundaries.

In vertical gradient freeze (VGF) method, the heaters and the growth ampoule are stationary, hence it allows the heat transport to be controlled and stabilized [30]. Crystallization can be achieved by programmatically ramping down the temperature of the hot and cold zones. By keeping a constant temperature, the melting point isotherm of the system is swept from the seeding position to the end of the growth ampoule. The VGF is the most cost-effective method of growing II-VI compound semiconductors, as it has the fastest crystal growth rate. The main differences between two methods are depicted in Figure 2.2. While in VBM three temperature zones (top hot zone, middle adiabatic zone and bottom cold zone) are used, only two zones are used in VGF. In VBM during growth, the ampoule moves slowly along the furnace (along fixed temperature zone 1 to 3), but in VGF ampoule is stationery and temperature is regulated (reduced slowly) during crystal growth. In both cases, ampoules are rotated on their axes for a uniform heat distribution.

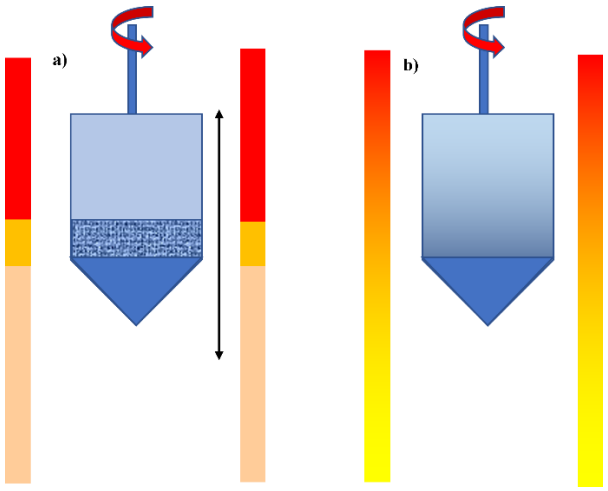

Figure 2.2 Schematic diagram showing differences for: (a) vertical Bridgman growth (VBM) and (b) vertical gradient freeze technique (VGF).

2.2 PRECURSOR MATERIAL PREPARATION

Charge carrier transport and optical absorption/transmission properties of crystals are significantly affected by the presence of trace level residual impurities in precursor materials. Therefore, high-purity materials with >5N purity (>99.999%) have become extremely important in growing detector quality semiconductor crystals. Quaternary CZTS compound was first grown for radiation detector in 2019 by Roy et al. at Brookhaven National Laboratory (BNL) [27] using THM growth method. They had used pre-synthesized 6N (99.9999%) purity $Cd_{0.9}Zn_{0.1}Te$ and CdSe precursor materials. Yakimov et al. at General Electric (GE) used horizontal Bridgman technique to grow CZTS from commercially available 6N purity CZT and 4N purity CdSe as precursor materials along with elemental Cd [29]. In this thesis, growth of CZTS single crystals using 7N (99.99999%) purity elemental precursors viz., Cd, Zn, Te, and Se instead of pre-synthesized precursors is reported.

To obtain 7N purity precursor materials, commercially available 5N purity elemental Cd, Zn, Te, and Se were purified using multi-pass horizontal zone-refining method as previously reported by our research group [31-33]. This method is based on the phenomenon that when a solid is melted impurities distribute differently in solid and liquid phases during solid-liquid transition [34]. Generally, solubility of impurities is greater in a liquid phase than in a solid phase. Thus, when a section of solid material is melted and the molten 'zone' is passed slowly through the entire solid material, the impurities transition from solid phase to liquid phase. On repeating this process multiple times (multi-pass zone refining), the resulting solid become extremely pure at one end, while segregated impurities accumulates at the other end of the solid. The effectiveness of zone refining depends on the ratio of the impurity concentration in the solid phase (C_s) and that in the liquid phase (C_l) at thermodynamic equilibrium. This ratio is known as the impurity segregation constant, k, where:

$$k = C_s/C_l \qquad 2.1$$

As expressed in the Equation 1, a k value <1 implies a more effective purification with the zone refining. A picture of zone-refining system used for the study is presented in Figure 2.3.

While conducting zone refining using the set-up in our lab, the precursor materials were vacuum sealed in a quartz ampoule and loaded into a single zone horizontal furnace mounted on a track actuator. The furnace temperature was increased up to slightly above the melting point of each precursor material. The furnace was horizontally moved along the ampoule length using the track actuator at a speed of 20 mm/day. A total of 40 passes were made, by the end of which most of the impurities were collected into one end of the

ampoule through segregation, and we were able to obtain ≥ 7 N purity material as determined by glow discharge mass spectroscopy (GDMS). After ending the zone-refining process, the pure end of refined ingot was separated from the impure end and preserved in an argon-controlled environment. The refined ingots of the precursor materials were stored in argon-filled polyethylene bottles in an argon-controlled glove box for growth experiments. The GDMS impurity analysis data of the zone-refined precursor elements are presented in Table 2.1.

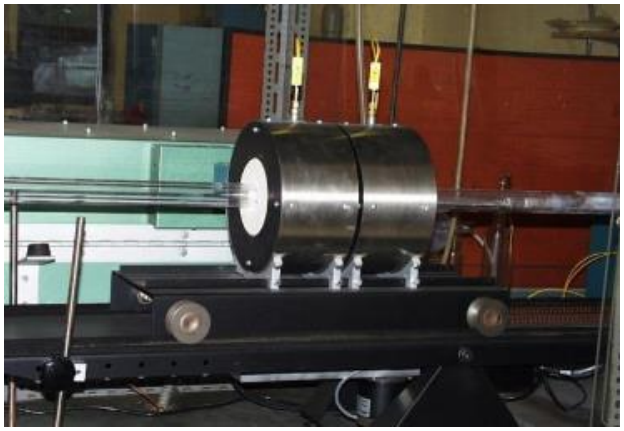

Figure 2.3 Zone refining set-up of our lab.

Table 2.1 Impurity concentration, in parts-per-billion (ppb), determined by GDMS analysis for zone refined elemental precursor materials for CZTS crystal [35].

Impurity	Cd	Zn	Te	Se
O	2.8 (< 0.5)	2.4 (< 0.4)	4.6 (< 0.6)	n/m
Na	1.5 (0.5)	1.7 (0.2)	1.6 (<0.4)	9.5 (<1.2)
Sn	1.5 (< 0.5)	1.6 (< 0.2)	1.2 (< 0.2)	12 (<0.5)
Al	2.3 (0.3)	1.4 (n/d)	1.6 (n/d)	2.2 (1.0)
Cd	Major	1.3 (0.3)	1.5 (0.3)	n/m
Li	4.1 (1.4)	4.5 (1.2)	2.2 (<0.3)	0.5 (<0.5)
Mn	5.5 (1.5)	1.2 (<0.3)	1.4 (<0.3)	1.0
Zn	1.2 (0.6)	Major	n/m	10 (1.0)
Te	4.4 (0.6)	0.6 (<0.1)	Major	8.0 (0.35)
Cu	4.2 (1.2)	2.4 (0.2)	1.6 (<0.3)	25 (0.2)
Pd	1.6 (<0.3)	1.5 (<0.2)	1.9 (<0.2)	n/m
Co	2.1 (<0.2)	1.9 (<0.4)	1.4 (<0.2)	1.0 (<0.2)
Ni	3.5 (0.3)	1.6 (n/d)	1.4 (n/d)	5.0 (0.2)
Fe	0.8 (0.2)	0.5 (n/d)	0.6 (n/d)	10 (n/d)
Hg	4.4 (0.3)	4.1 (<0.5)	4.5 (<0.3)	7.0 (<0.4)
Si	5.4 (1.6)	2.5 (0.6)	2.3 (1.2)	5.0 (<0.4)

Note: The values outside the parenthesis are for a material before zone refining and values within the parenthesis are for the same material after ZR showing the effectiveness of ZR process. “n/m” is not measured.

2.3 CARBON COATING

Generally, quartz ampoules are used for crystal growth due to their resistance to high temperature and pressure. The differences in individual precursor material’s properties such as melting point, vapor pressure, thermal conductivity can result in difficulties of growing detector-grade compound semiconductors. For example, due to its low melting point (321.1 °C) and high thermal conductivity (0.9 W/cm^{-1} K^{-1}), cadmium (Cd) tends to adhere to the inside wall of the quartz ampoule. In the presence of oxygen,

cadmium forms cadmium oxide (CdO), which further reacts with the silicon in the quartz ampoule to form cadmium metasilicate ($CdSiO_3$) making growth ampoule very fragile. To prevent formation of this compound, interior walls of the quartz ampoule is coated with carbon [36]. Carbon at elevated temperature react with any residual oxygen or adsorb water within the ampoule, resulting in the formation of carbon dioxide or carbon monoxide.

Carbon coating on quartz ampoule was performed in our lab by inserting a conically tipped quartz ampoule (ID: 16 mm and OD: 20 mm) with a wall thickness of 2 mm in the in-house carbon coating set up. The ampoule was purged with argon at 950 °C for half an hour, to remove any residual air molecules in the ampoule. N-hexane vapors at a rate of 7 mL/min for 8 hours was passed under argon flow at 950 °C. The carbon-coated ampoule was then annealed at 1100 °C for 3 hours under argon atmosphere. Figure 2.4 shows the tube furnace used for carbon coating and Figure 2.5 shows a quartz ampoule before and after carbon coating. Growth ampoule has cylindrical shape with conical tip that hosts seed crystal and allows unidirectional synthesis.

Figure 2.4 Tube furnace used for carbon coating in our lab.

Figure 2.5 Carbon coated (a) and uncoated (b) quartz ampoule.

2.4 VERTICAL BRIDGMAN GROWTH METHOD

The CZTS crystals are grown from zone-refined 7N (99.99999%) purity precursor materials (Cd, Zn, Te and Se) in $Cd_{0.9}Zn_{0.1}Te0._{97}Se_{0.03}$ atomic ratios with 5% excess Te by weight. The melting point of CZTS precursors are 321.1°C for Cd, 419.6°C for Zn, 449.5°C for Te, and 220°C for Se, whereas melting point of CdZnTe compound is reported to be about 1120°C. So, an elevated temperatures ≥1100°C will be needed to grow CZTS crystals. However, Cd vapor pressure at elevated temperature >1100°C creates the possibility of an explosion. To mitigate this, an excess tellurium (Te) is used during crystal growth allowing crystal growth to occur in solvent medium at a temperature about 980°C [37]. It also mediates the compositional fluctuations that arise due to large difference in the melting points of Cd and Te. To grow CZTS crystals, first, zone-refined elemental precursors were weighed and loaded into the carbon-coated quartz ampoule (Figure 2.5). To remove any residual moisture, the loaded quartz ampoule was heat treated at 110°C and kept overnight under high vacuum (10^{-6} Torr). The ampoule was then sealed under a vacuum of 10^{-6} Torr using an appropriate quartz plug fused to the inner wall of the tube by an oxyhydrogen flame. Figure 2.6 shows quartz ampoule sealing system and an ampoule loaded with precursor materials being heat treated prior to sealing.

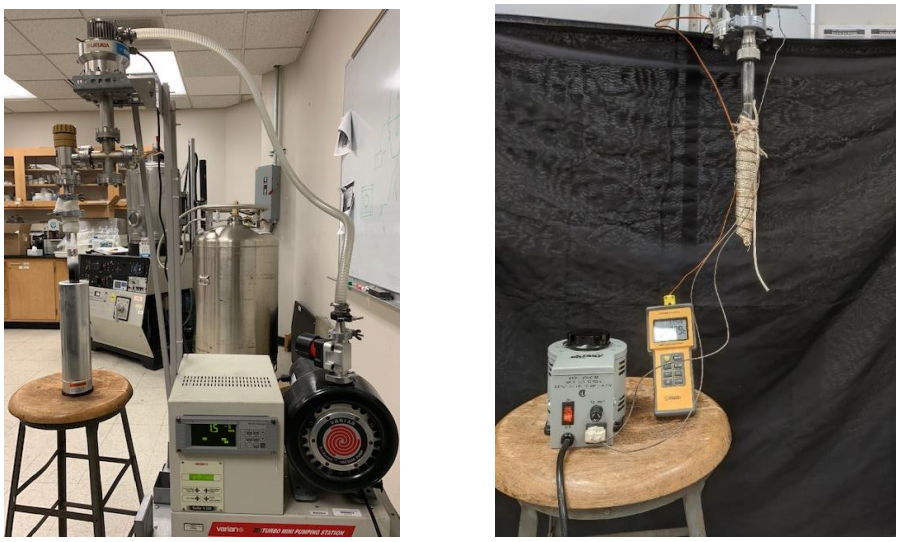

Figure 2.6 Quartz ampoule sealing system at our laboratory for growing CZTS crystals (left) and the growth ampoule being heat treated for sealing (right).

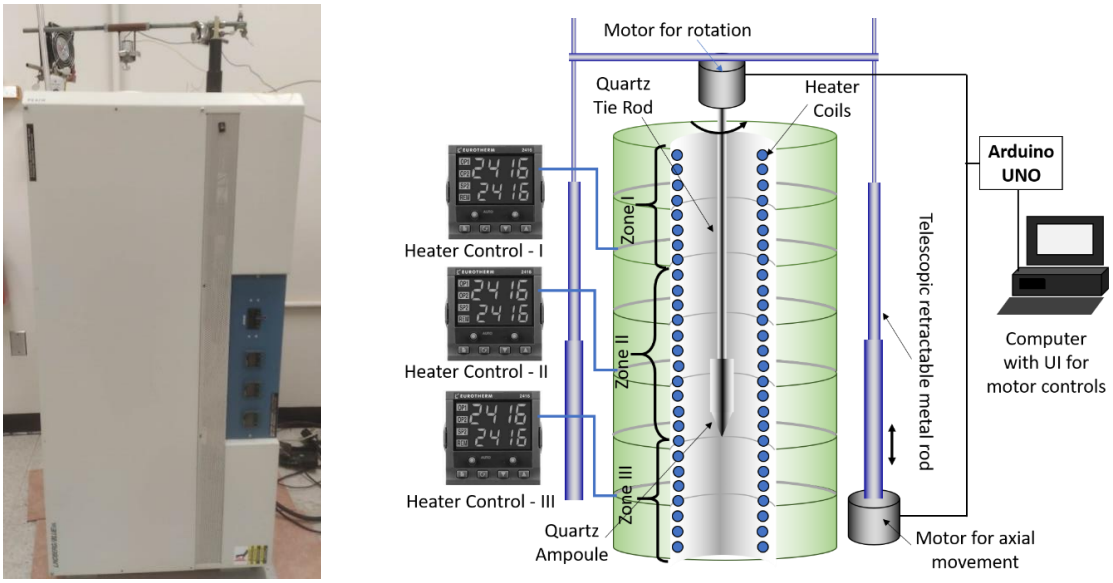

Figure 2.7 Picture of a Lindberg Blue growth furnace used for this study (left) and a schematic diagram of vertical furnace arrangement used for CZTS crystal growth (right).

A three-zone Lindberg Blue furnace (Figure 2.7) modified for vertical Bridgman growth was used to grow CZTS crystal. A rod attached to the actuator was extended through the center of the furnace to hold the growth ampoule. An h-bridge setup controlled

the speed and direction of the actuator. The sealed carbon coated quartz ampoule with precursor materials was loaded inside the growth furnace and then slowly heated to synthesize CZTS compound. Heat treatments were performed at 950 (zone 1), 980 (zone 2) and 975 °C (zone 3) for 3 h to synthesize the charges directly from the elements with addition of excess Te. During synthesis, a small motor, controlled by an Arduino micro-controller, rotated the ampoule at a speed of 15 rpm for a uniform heat distribution throughout the melt to achieve radial compositional homogeneity. The furnace was programmed and controlled to achieve the desired temperature profile. Figure 2.8 shows the programmed growth profile for CZTS and a cross-sectional view of the furnace showing COMSOL simulated steady state temperature distribution. The temperature gradient across the furnace zones and the axial temperature profile has been verified manually using a thermocouple and shown in Figure 2.9. The furnace was ramped up to the peak growth temperature of 980 °C in various stages, with progressively slower ramp rates, to avoid any back stress at the solid–liquid interface resulting from thermal expansion coefficients. An axial temperature gradient of 3.5 °C/cm was maintained. The ampoule was moved downward at a constant velocity of 3 mm/hour for directional solidification of the grown crystal. At the end of the growth run, the furnace was slowly cooled down, once again at various ramp rates with progressively faster rates. This was done to avoid any thermal stress on the ampoule and to allow the uniform solidification of the grown crystal.

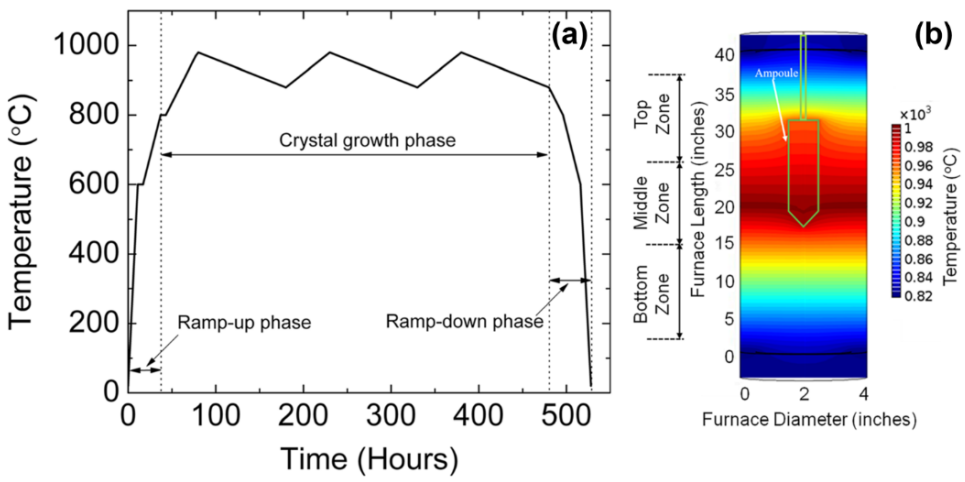

Figure 2.8 (a) The programmed growth profile of CZTS crystal. (b) The cross-sectional view of the furnace showing simulated steady state temperature distribution.

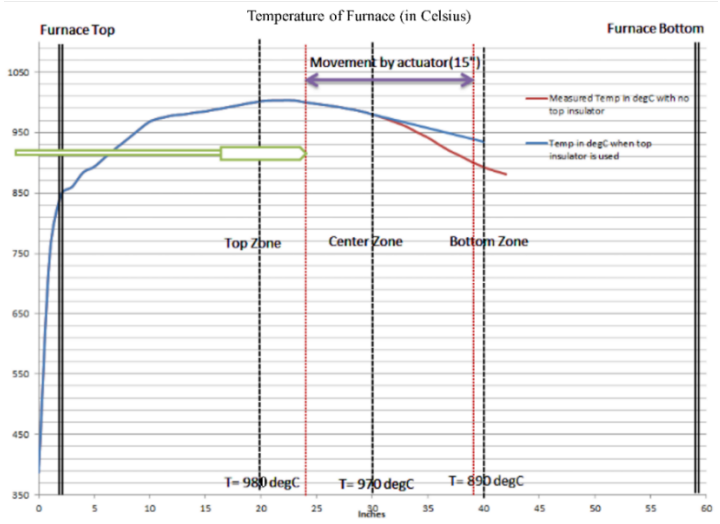

Figure 2.9 The temperature profiles for the modified vertical Bridgman method.

2.5 VERTICAL GRADIENT FREEZE GROWTH

For vertical gradient freeze (VGF) technique, the precursors and the growth ampoule were prepared the same way as it was done for vertical Bridgman growth method and described in above section. As in Bridgman growth, an excess of 5% tellurium (Te)

was added to the precursor materials; in addition to that ~15 ppm compensating Indium (In) of 7N purity was used as a dopant to achieve high resistivity.

CZTS crystal growth by VGF was performed using the upper two zones of the Lindberg Blue crystal growth furnace (Figure 2.7): zone 1 (hot zone) situated at top and zone 2 (cold zone) situated at the middle of the furnace ~20 inches apart from zone 1. The ampoule was placed within the zone 1 while the tip was placed at the level of zone 2 heating element. During the growth process, zone 1 was slowly ramped up at various temperature rate, to its peak temperature of 985°C, care had been taken to ensure that there were no issues caused by cadmium vapor pressure, while zone 2 was ramped up and maintained at 960°C creating a thermal gradient between the two zones. Both zones were held at these temperatures for 72 h to ensure homogeneous mixing of the melt. After 72 h, both zones were slowly ramped down at 5°C/h until the top zone reached 850°C, after which it was ramped down at a rate of 10°C/h till it reached 600°C. Following this, the furnace was allowed to free fall reaching room temperature in ~8h. Figure 2.10 (a) shows a 3D schematic of the VGF furnace used for the crystal growth and a simulated steady state temperature distribution (using COMSOL) inside the furnace at peak temperatures of the two zones (985°C/960°C). Figure 2.10 (b) illustrates a two-dimensional cross-sectional view of the furnace and the temperature profile showing the thermal gradient between zone 1 and zone 2 under the same conditions. According to the simulation, the temperature of the ampoule tip was ~965°C.

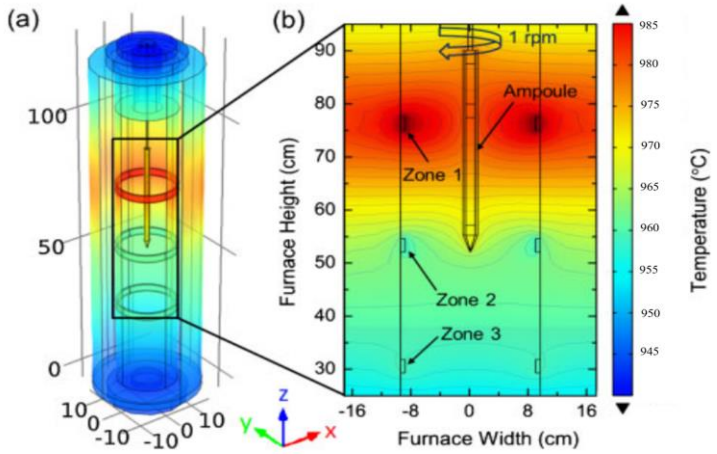

Figure 2.10 (a) 3D schematic of the VGF furnace showing simulated temperature distribution under steady state at peak temperatures of (985°C/960°C) for (zone 1/zone 2), and (b) cross-sectional view of the furnace showing thermal gradient between the two zones and around the ampoule.

2.6 CZTS CRYSTAL PROCESSING

After crystal growth, grown CZTS ingot was taken out from the ampoule and cut into several wafers using Extec Labcut 150 wafer cutter (Figure 2.11-a). The grown ingots contained patches of single crystal regions called grains. For detector fabrication, the wafers are visually inspected to identify the bigger grains, as bigger the grain sizes are, larger the detector blocks could be fabricated. Figure 2.12 shows photographs of an as-grown CZTS ingot and a cross-sectional view showing large grain boundaries. After cutting, the wafers are grounded and lapped mechanically starting with coarse sandpaper down to 1500 grit SiC paper, and polished using alumina powder and water-slurry down to 0.05 µm alumina powder. The polished wafers are then thoroughly cleaned using deionized water to clean off any residual alumina powder. For reducing the effects of surface oxides and any defects caused by mechanical polishing, the wafer surfaces were chemo-mechanically polished (CMP) and etched using 2-5% bromine-methanol solution

(Br_2/MeOH) for 1 min. Polished and etched CZTS crystals slices were then used to fabricate pixelated and planner devices to evaluate electrical and spectroscopic properties of CZTS crystals. Planar geometry generally implies a linear electric field across the detector thickness when biased and are required for resistivity and charge transport property measurements described in the next chapter.

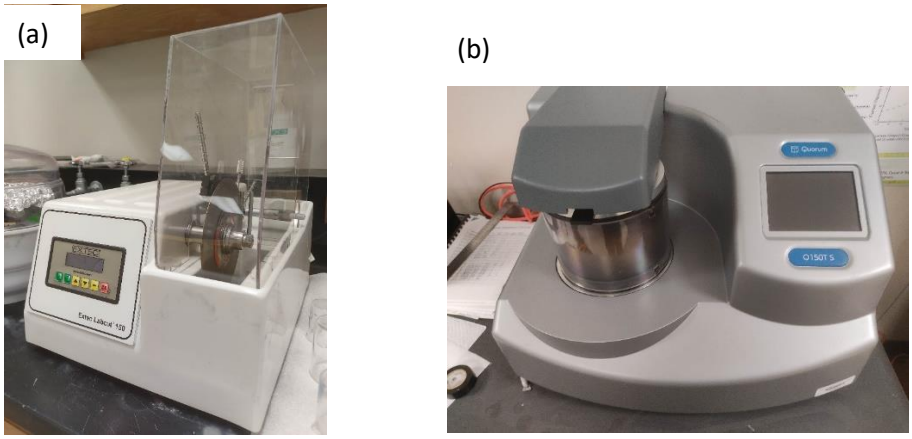

Figure 2.11 (a) Extec Labcut 150 diamond saw, used for cutting CZTS crystals. (b) Quorum Q150T sputtering unit.

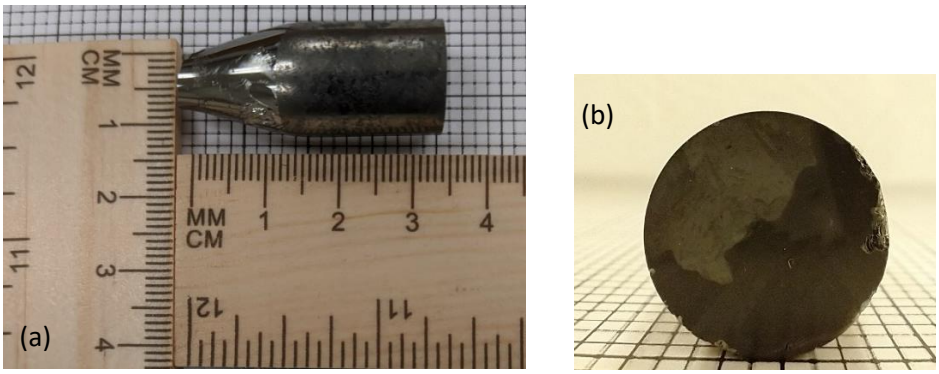

Figure 2.12 (Left) Photograph of as-grown CZTS ingot; (b) Cross-sectional view of a CdZnTeSe ingot with large grain boundaries.

A schematic diagram of the CZTS detector device is shown in Figure 2.13. This simple device consists of a gold (Au) top pixel electrode and a gold (Au) planar bottom electrode (~90 Å thick). Using Quorum 150T RF-DC sputtering unit (Figure 2.11 -b), gold metal contacts (electrodes) were deposited on two opposite CMP-polished surfaces to obtain planar detector geometry. A shadow mask on the sample was used allowing deposition of metal exactly the dimension or position as intended. Figure 2.14 shows photographs of polished wafers with gold contact in small pixel and planar geometries. The dimension of the wafer used for the present study is 11.0 × 11.0 × 3.0 mm^3.

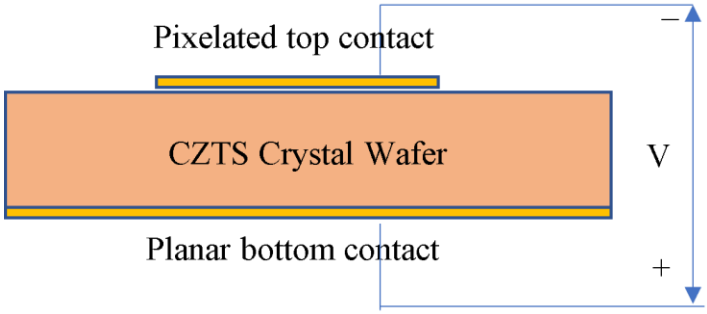

Figure 2.13 Schematic of the fabricated CZTS device

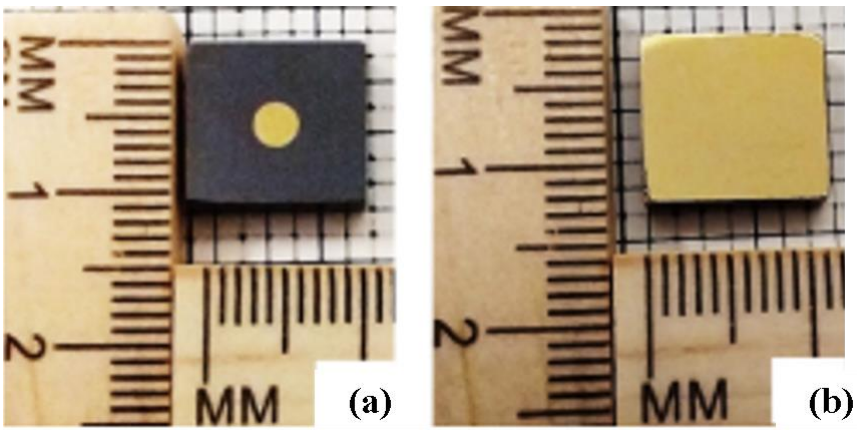

Figure 2.14 Polished CZTS wafers (11.0 × 11.0 × 3.0 mm^3) with gold contact configured as a small pixel (a) and a planar detector (b).

CHAPTER 3

CRYSTAL CHARACTERIZATION

3.1 OVERVIEW

This chapter describes experiments and results of various measurements carried out to evaluate grown CZTS crystal for its morphology, composition, crystallinity, and electrical properties. These characterizations are important to make certain that grown CZTS semiconductor crystal display certain characteristics of effective radiation detector materials as listed in Table 1.1. First, x-ray diffraction (XRD) study was carried out to confirm that the grown CZTS crystal has zinc blend lattice structure as expected; crystallographic planes and lattice constant of the CZTS crystal were determined. Energy dispersive x-ray spectroscopy (EDX) was carried out to confirm the formation of intended stoichiometry (compositional characteristics) of the grown CZTS crystal. Prior to device fabrication, surface morphology of polished and etched CZTS wafers were studied using scanning electron microscopy (SEM) to confirm the wafers has desired large grain-boundaries and free of surface defects. X-ray photoelectron spectroscopy (XPS) was carried out to investigate elemental compositions especially at the surface of the polished wafers. Finally, electrical characterization was performed using current-voltage (I-V) measurements to determine resistivity, leakage current, and Ohmic or Schottky behavior of semiconductor-metal junction.

3.2 X-RAY DIFFRACTION

X-ray diffraction (XRD) uses the electromagnetic radiation in the wavelengths from 0.01 to 10 nanometers (x-ray range), to categorize and measure physical properties within a crystalline structure. The information is gathered by bombarding x-rays onto a structured material and measuring the reflected or transmitted x-rays. XRD works on the principle of Bragg's equation stated as,

$$n\lambda = 2dsin\theta \tag{3.1}$$

where n is a whole number for constructive interference, λ is the wavelength of x-rays, d, is the spacing between layers of atoms, and θ, is the angle between the incident rays and the surface of the crystal. Since materials have varying lattice spacing, arrangement, and composition, they diffract the incoming x-ray beam at different angles. These angles are then plotted with respect to their intensities. When an intensity peak shows up, due to the constructive interference satisfying the Bragg's equation, information such as material characteristics and lattice structure can be determined.

The CZTS crystals grown using both vertical Bridgman method (VBM) and vertical gradient freeze (VGF) techniques were characterized by powder XRD method using a Rigaku D/MAX 2100 powder x-ray diffractometer (CuKα radiation, λ = 0.15406 nm). The crystal quality, preferential orientation, and crystal structure as well as the lattice constant of the grown crystal was evaluated. The sample was prepared for XRD measurement by grinding the as-grown crystal into fine powder (few microns large) using a mortar and pestle. The obtained XRD pattern of the powdered VBM grown CZTS crystal is shown in Figure 3.1. A strong diffraction peak was obtained at 2θ angles of 23.89°, 39.53°, and 46.53° corresponding to (111), (220), and (311) crystal planes, respectively. The sharp diffraction peaks with small FWHM confirms high quality single crystalline nature of the

grown material. The peaks were compared to the standard CZT XRD pattern (ICSD#620556), as both are similar in their nature of having a zincblende structure. The XRD peaks found in grown CZTS crystal agrees with XRD peaks of the reference CZT sample. Assuming that the powdering of the crystal did not disturb the atomic arrangement within particles of the powder, the XRD result suggested that the grown crystal had their strongest peak in the (111) plane, with a centroid of $2\theta = 23.89°$.

The Gaussian fit was performed for the strongest peak - (111) plane, and a full width half maximum (FWHM) of ~0.192° was obtained. The lattice constant was calculated using the equation,

$$a = \frac{d_{hkl}}{\sqrt{h^2+k^2+l^2}} \qquad 3.2$$

where d_{hkl} is the d-spacing of the crystal atoms, obtained by Bragg's equation (Equation 3.1). The lattice constant a, corresponding to the (111) plane was calculated to be 6.447 Å, which is similar to previously found values in CZT samples.

Figure 3.2 shows the x-ray diffraction pattern of CZTS single crystal grown using VGF method. For this case also the predominant crystal plane (the strongest peak) was (111) which was located at $2\theta = 24.71^{\circ}$, which shifted slightly from the 2θ angle observed for VBM grown CZTS sample. This sample too exhibited sharp diffraction peaks suggesting high quality single crystal nature of the grown material. The crystallinity was calculated to be 88.7%. The lattice constant found from the XRD was a = 6.42 Å, which is in good agreement with the VBM grown crystal and standard value a = 6.424 Å (JCPDS # 00-053-0552) and a = 6.431 Å (JCPDS # 00-041-1324) for zinc blend lattice of CZT matrix. All other major diffraction peaks corresponding different crystal planes are indexed in XRD figures given below.

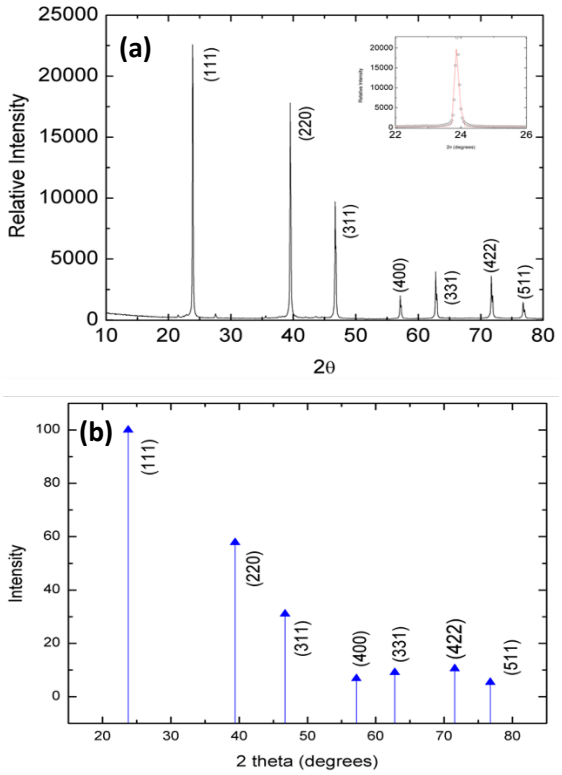

Figure 3.1 (a) Powder diffraction patter of the CZTS ingot grown by VBM method. Inset shows the Gaussian fit of the (111) plane. (b) Reference pattern of $Cd_{0.9}Zn_{0.1}Te$ sample (ICSD#620556)

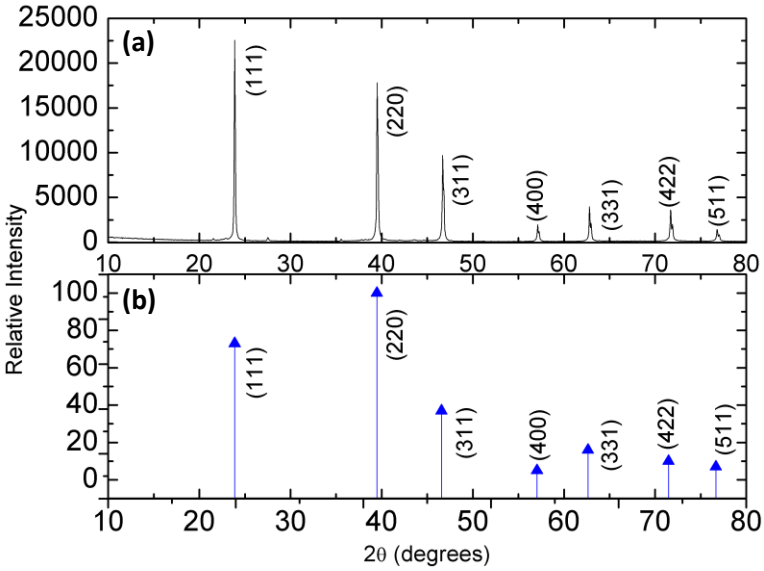

Figure 3.2 (a) Powder diffraction patter of the CZTS ingot grown by VGF method showing different XRD peaks corresponding crystal plane. (b) XRD pattern of CZT reference sample.

3.3 STOICHIOMETRY DETERMINATION BY SEM-EDX

Elemental composition and the stoichiometry (Cd, Zn, Te and Se atomic ratio) of the grown CZTS crystals were examined by scanning electron microscopy (SEM) energy dispersive x-ray spectroscopy (EDX, SEM-EDX). The scanning electron microscope flashes focused beams of high-energy electrons into the material and these electrons collide with inner shell electrons of crystal lattice providing enough energy to emit x-ray photons. These x-rays have unique energy based on the element composition, structure, crystalline orientation, etc. This energy is converted into a voltage signal that is then "counted" by a software program. This program then graphs the data and the locations of the energy peaks that revels the material composition.

Prior to SEM-EDX analysis, the sample surface was prepared by mechanical polishing with alumina suspension to obtain a mirror finish. The sample was then etched by dipping in 0.5% Br_2/MeOH dip for 20 seconds. It was then rinsed with ultrapure isopropanol and finally dried by blowing pure nitrogen.

The compositions were determined by SEM-EDX using a high resolution Tescan Vega 3 SBU Scanning Electron Microscopy (SEM) equipped with EDX integration software. The SEM was attached with the EDX system so that the sample could be viewed to select the sample position for analysis. The analysis was carried out in different places of the wafer to confirm the uniformity of the compositional stoichiometry in the grown crystals. The quantitative analysis was carried out by comparing the intensity (the number of x-ray photons per second) of the x-ray emission from the CZTS sample being examined

with that from a standard pure element. The 7N (99.99999%) purity of the precursor materials were taken as standard reference.

The EDX spectrum in Figure 3.3 shows the presence of all the elements in CZTS compound (Cd, Zn, Te, and Se) with no indication of impurity elements within a margin of 7N. The weight percentages and the atomic percentages were observed across various points in the crystal and appeared to be similar across all points indicating a good homogeneity across the crystal surface. The average values of EDX measurements for the CZTS crystal wafers are listed in Table 3.1. The selenium to tellurium atomic ratio was found to be 0.03 for both CZTS samples (VBM & VGF) as expected. The cadmium to tellurium atomic ratio was found to be 0.90 for VBM grown CZTS sample while that for VGF grown sample was found to be 0.83. These values were close to the expected value Cd/Te atomic ratio of 0.93 for intended stoichiometry of $Cd_{0.9}Zn_{0.1}Te_{0.97}Se_{0.03}$. The slightly lower than expected cadmium to tellurium atomic ratio for VGF grown CZTS sample shows some inhomogeneity in grown crystal and probably resulted from slightly inconsistent growth temperature or high cadmium vapor pressure.

Table 3.1 Compositions of CZTS crystals as determined by SEM-EDX comparing the weight percentage and the atomic percentage of the crystals grown by vertical Bridgman technique and vertical gradient freeze technique.

Sample #	**Cd Content (%)**	**Zn Content (%)**	**Te Content(%)**	**Se Content(%)**
VBM (at %)	44.76	3.88	49.46	1.90
VBM (wt %)	42.83	2.16	53.73	1.28
VGF(at %)	43.19	3.23	52.21	1.36
VGF(wt %)	41.02	1.78	56.29	0.91

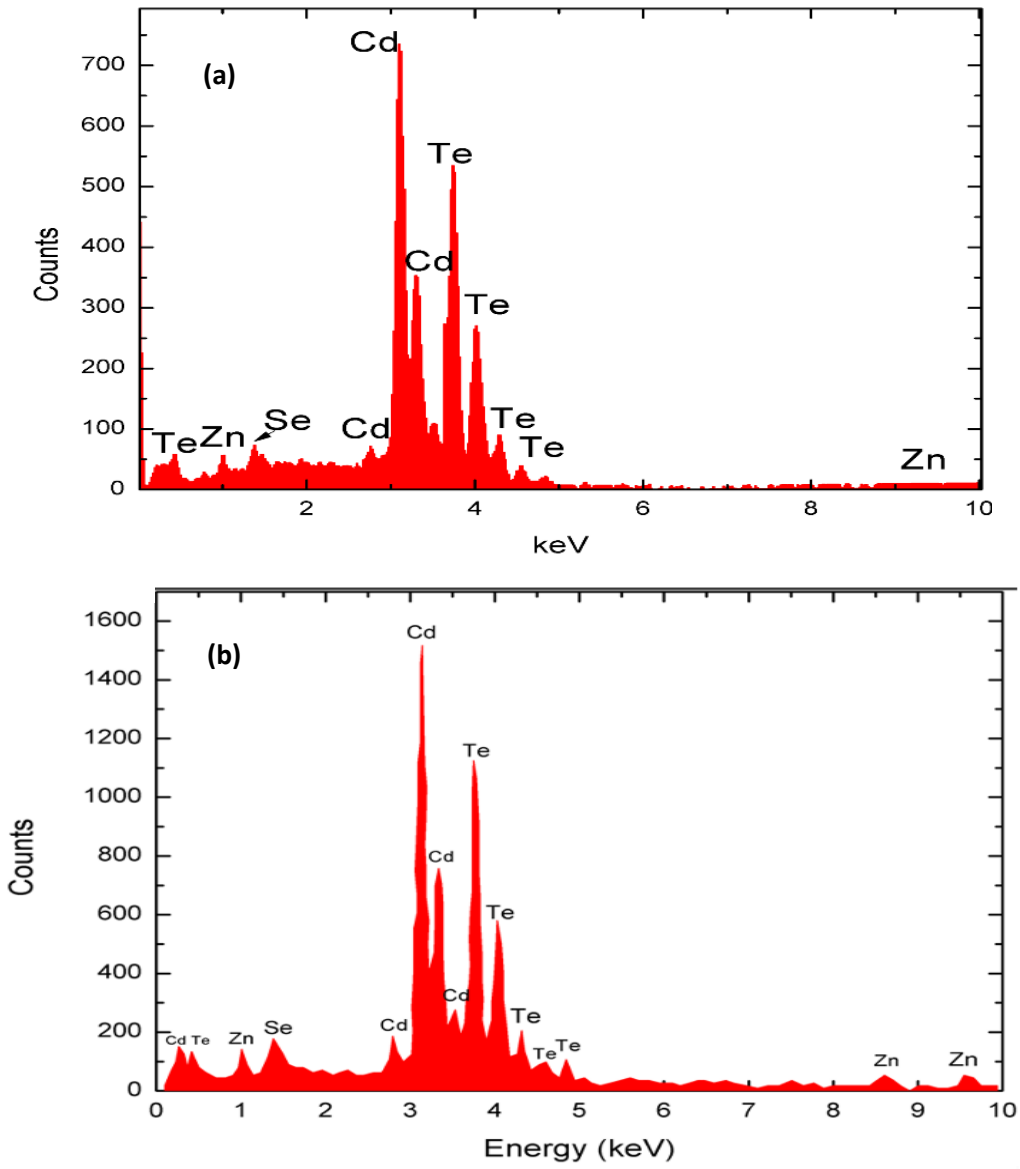

Figure 3.3 Energy dispersive x-ray spectra of grown CZTS crystal using (a) VBM growth method and (b) VGF growth method.

Surface morphology study was carried out using scanning electron microscopy (SEM) and high-resolution optical microscope to investigate the various crystallographic defects or irregularities such as grain boundaries, twins and dislocations generated during

the crystal growth and subsequent crystal processing. The same SEM setup as in SEM-EDX study described above was used here. SEM studies on chemically etched CZTS wafters showed smooth surface morphology without visible defects or microcracks. The SEM image of CZTS crystal grown using VBM growth method is shown in Figure 3.4. The SEM measurements have been carried out on the same samples that have been used for detector fabrication for electrical characterization and pulse height spectroscopy.

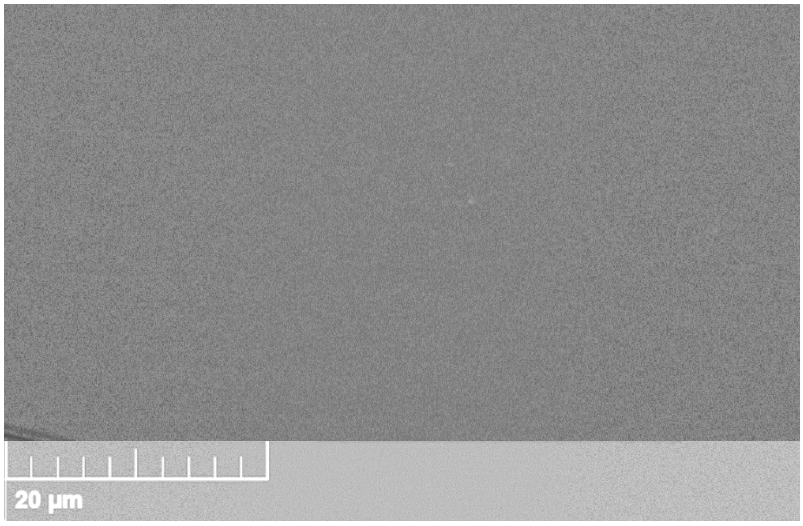

Figure 3.4 SEM image of CZTS wafer after polishing and etching.

3.4 SURFACE STUDY BY XPS

X-Ray Photoelectron Spectroscopy (XPS) is a measurement used to analyze the surface chemical composition of semiconductor crystals and devices. In this method the surface is bombarded with monoenergetic soft x-ray radiation (generally MgKα (1253.6eV) or AlKα (1486.6eV) are used as the x-ray source), resulting in emission of electrons by the photoelectric effect. The energy of emitted electrons is then measured. Depending on the atoms they were emitted from, these emitted electrons have different

characteristic energy. To eject an electron into the vacuum with kinetic energy E_k, having a spectrometer work function Φ, an incident photon must have high enough energy hν to ionize an electron bound within an electronic shell according to:

$$E_k = h\nu - E_B - \Phi \qquad 3.3$$

The incident radiation is a monochromatic (a single wavelength) light of a known energy, spectrometer work function Φ is known quantity, and measurement of E_k can be conducted using an electron energy analyzer. Therefore, using Equation 3.3, binding energy E_B can then be calculated. As the level of radiation contains enough energy to ionize core levels of most elements, studies involving both the band states as well as the core states can be performed. This is analyzed by a peak seen in the photoelectron energy distribution and shows a presence of a particular element within the structure. If the inner electronic and nuclear energy levels shift, the atoms indicate a change in its chemical state. Detecting these changes of the electronic energy levels provides information on the type of chemical bond the atom has with its neighboring atoms.

XPS was conducted by a Kratos AXIS Ultra DD system that included a hemispherical energy analyzer and a monochromatic AlK_α source. This source was operated at 15KeV with a 150W surface incidence at 45^o. The binding energy of the analyzer was calibrated with an Ag foil to the value of 368.21 ± 0.025 eV. The surface area for analysis area of the VBM grown crystal was around 0.3 mm x 0.3 mm. All measurements were taken under an ultra-high vacuum at 2×10^{-9} Torr.

Figure 3.5 shows the XPS scan survey for the unmodified as-grown CZTS sample; photoelectron peaks of interest are identified and indexed. The survey shows the typical strong spectral lines previously observed for CdTe and CZT for Cd, and Te. Additionally,

the *2p* level for Zn and *3d* level for Se can also be observed. C and O were introduced on the sample surface after growth and were unavoidable since the ingot was handled under ambient environment during characterization.

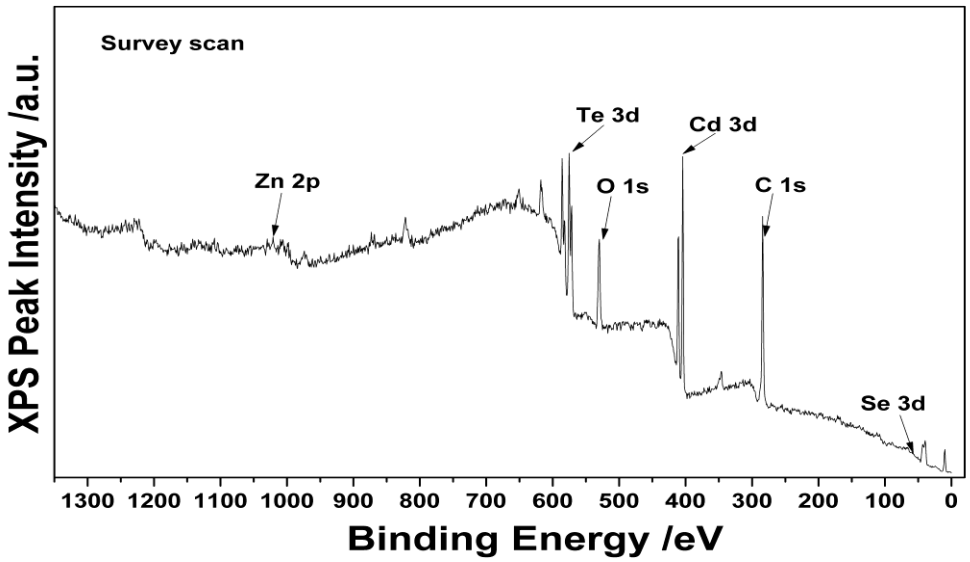

Figure 3.5 XPS survey scan of the grown CZTS sample.

Figure 3.6 (a) shows the high-resolution XPS scan of the Cd 3d core levels of CZTS sample. It is observed that the Cd 3d orbital split into two spin orbitals ($3d_{3/2}$ and $3d_{5/2}$). The Cd $3d_{3/2}$ core level peaks all exist at ~411 - 412 eV, while Cd $3d_{5/2}$ peaks reside at ~405 eV, which agrees with typical reported values for CdTe and CZT [38-39]. The $Cd_{5/2}$ peak signifies the formation of Cd-Te bonds (for Cd^{2+} state).

Figure 3.6 (b) shows the high-resolution spectra for the Te 3d core levels for the CZTS samples. The splitting of the 3d orbital to $3d_{3/2}$ and $3d_{5/2}$ spin orbitals located at ~583 eV and ~572 eV, respectively, was observed. This is consistent with reported Te 3d levels [38] and is caused by the Te-Cd bonds (the Te^{2-} state) [40]. Two additional peaks

were observed in the spectra of the CZTS sample at ~586 eV and ~576 eV, which are associated with O-Te bonding (for the Te^{4+} state) caused by TeO_2 [41-42].

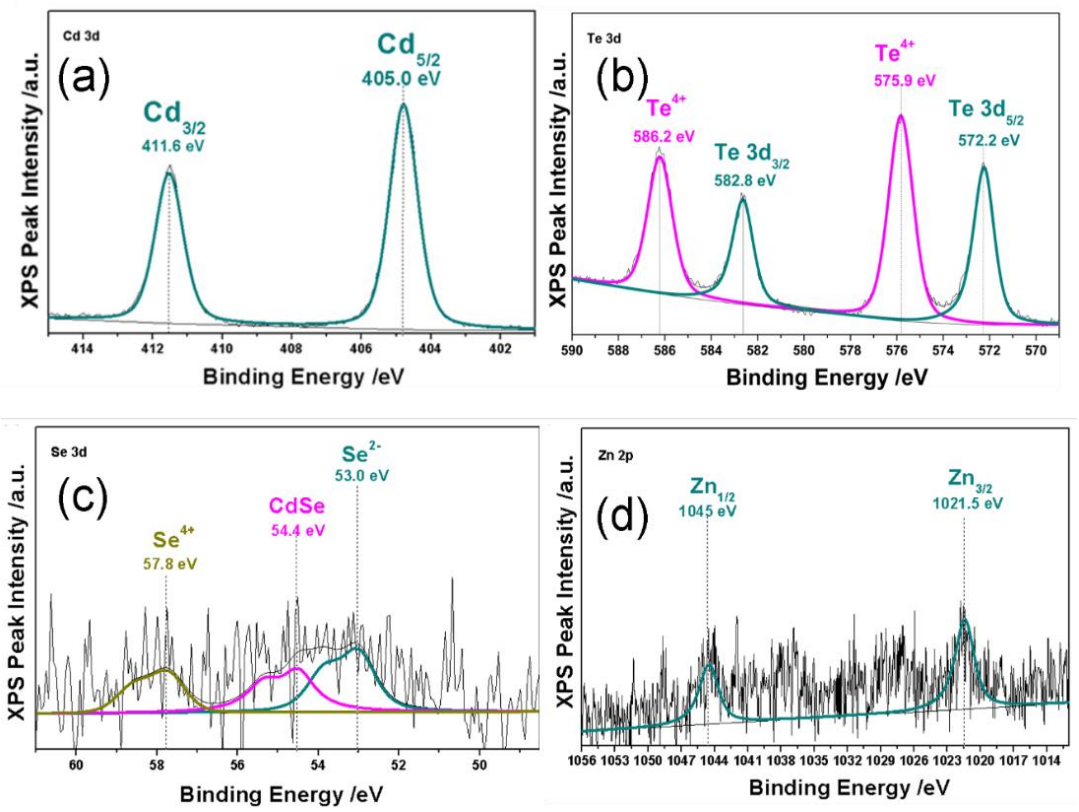

Figure 3.6 High resolution core level spectra of (a) Cd 3d, (b) Te 3d, (c) Se 3d and (d) Zn 2p.

Figure 3.6 (c) shows the splitting of Se 3d orbital which gives rise to three Se states. At 53 eV we observe Se $3d_{5/2}$ orbital which corresponds to an oxidation state of Se^{2-}. At 54.4 eV, the $3d_{3/2}$ spin orbital corresponding to a formation of Se-Cd bonding was observed. There is also a spectral distribution at 57.8 eV which corresponds to Se^{4+} state. Figure 3.6 (d) shows the spectral distribution of the 2p orbital of Zn into $2p_{1/2}$ and $2p_{3/2}$ at ~1045 eV and ~1021.5 eV respectively. The results suggest that the crystal orientations

and the elemental compositions were the same as intended. Other than unavoidable peaks of oxygen and carbon, there were no other impurity peaks.

3.5 ELECTRICAL CHARACTERIZATION

The surface morphological and the compositional characterizations of the grown CZTS showed physical properties that could affect the electrical properties in different ways. The current-voltage (I-V) characteristic is the basic electrical measurements that shows the relationship between the current through the device under an applied voltage across the device. The shape of the current-voltage (I-V) curve provides information regarding charge carrier transport through the semiconductor materials. The simplest I–V characteristic can be defined by Ohm's law which exhibits a linear relationship between the applied voltage and the resulting electric current involving a resistor (given in equation 3.4). The conduction type of the semiconductor material can also be indirectly inferred using I-V relationship. The quality of a device such as its leakage current and resistivity (as shown in equations 3.5 and 3.6) can also be easily determined by the I-V curve.

$$R = \frac{V}{I} \tag{3.4}$$

$$R = \rho \frac{L}{A} \tag{3.5}$$

$$\rho = \frac{V}{I} \cdot \frac{A}{L} \tag{3.6}$$

where, R is resistance in Ohm, V is voltage in Volt, I is current in Amp, ρ is the resistivity in Ohm-cm, A is contact area (cm^2) and L is the thickness of the device.

CZTS detector devices was fabricated on $11.0 \times 11.0 \times 3.0\ mm^3$ polished and etched wafer by depositing a gold circular electrode (single pixel) for top contact and planar gold

electrode (continuous) for bottom contact as shown in Figure 2.14. Standard planar detector configuration was used as this provides ease of fabrication. The detector fabrication process has been described in section 2.6 in the previous chapter. In a metal-semiconductor junction, the current-voltage characteristics are determined by the barrier height at the interface. Contacts on the semiconductor can either produce linear or rectifying response in the current voltage characteristics, depending on whether we have an Ohmic or a Schottky contact. Due to the large work function of CZTS, very few metals can be used to produce an Ohmic contact on CZTS. As gold (Au) has a high work function of 4.8 eV, it is an ideal candidate for p-type contact in CZTS semiconductor.

The current voltage measurements were carried out using a Keithley 237 source-measure unit with the detector in planar configuration. The detector was mounted on a printed circuit board (PCB) with copper pads for the bottom electrical contact. The top electrical contact was accomplished using a spring type contact attached to the PCB. The PCB was equipped with board-to-board connector pins. The PCB with the mounted detector acts like a modular device which can be plugged in and out of the test box for various measurements without disturbing the crystal. The test box is an electromagnetically shielded light-tight metal box fitted with BNC/Triax/SHV connectors for various electrical connections.

The plot in Figure 3.7 (a) shows the variation of leakage current as a function of bias voltage in CZTS detector with planar electrode configuration. This CZTS crystal was grown using modified vertical Bridgman growth method (VBM). The leakage current was observed to be few nanoamperes for a bias voltage of +200 V applied to one of the electrodes, whereas for - 200 V, the leakage current was measured to be 50 nA on the same

electrode. The current–voltage (I-V) characteristics showed higher asymmetry with respect to the bias polarity. The asymmetry in the I-V characteristics with respect to the bias polarity is mostly due to the different surface properties (dangling bonds, surface, and interface states etc.) which in turn leads to different surface carrier recombination velocities [41, 43-44]. The bulk resistivity has been calculated from a low voltage range I-V characteristic and has been found to be ~ 10^{10} Ω-cm which is needed to form high performance gamma radiation detector.

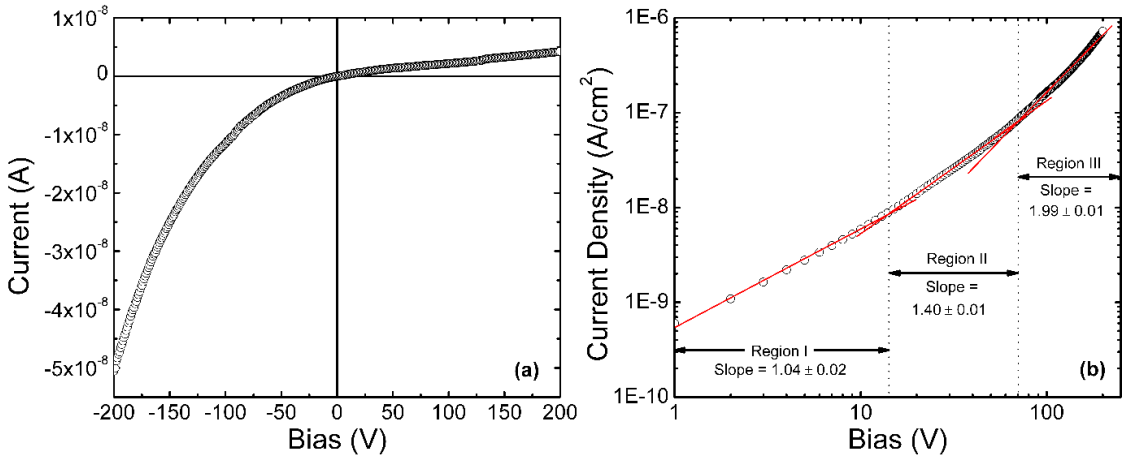

Figure 3.7 (a) Variation of leakage current as a function of bias voltage in a planar VBM grown CZTS detector measured at room-temperature and under dark. (b) The negative polarity *I-V* curve has been replotted as log *J* – log *V* plot. The solid red lines are the linear fits to the log *J* – log *V* curves; slopes of the linear fits are mentioned within the plots.

Figure 3.7 (b) shows the log–log plot of current density *J* as a function of the negative bias voltage *V*. The plot shows three different linear regions; each of them was fitted with a straight line. The slopes of the three linear regions varied from 1 to 2. Only the slope of the first region (0–15 V) is close to unity (=1) suggesting an Ohmic type current flow. A higher than unity value for the slopes of linear fits in second and third regions implies that at the higher bias the device did not exhibit linear relationship between the applied bias and leakage current.

In Ohmic conduction, the current is mainly driven by the mobile charge carriers being intrinsically present in the device material. At higher bias voltages, a large number of electrons are injected into the semiconductor from the contacts and the concentration of the injected carriers at equilibrium becomes much larger than that of the intrinsic carrier concentration. In this condition, the current-voltage characteristics become quadratic ($I \infty V^2$) and the current, known as space-charge limited current (SCLC), becomes dependent only on the mobility as is expressed by Eq. 3 below [45, 46]:

$$J_{SCLC} = \frac{9}{8}\mu\varepsilon\frac{V^2}{d^3} \qquad 3.7$$

where ε is the electrical permittivity of CZTS, μ is the drift mobility of the charge carriers, and d is the thickness of the detector. It is obvious from equation 3.7 that the slope of log *J*–log *V* plot in such a condition would be 2. The region III of the log *J*–log *V* plot in Figure 3.7 (b) with a slope of ~ 2 most likely corresponds to the SCLC regime.

It is to be noted that in the case of presence of shallow traps, the drifting charge carriers are repeatedly trapped and de-trapped from the shallow traps, in which case the mobility μ in the above equation becomes the effective reduced drift mobility. The region II may be related to trap SCLC, where defects play a role as recombination centers which leads to slower rise in current with increasing bias voltage [47].

The current-voltage characteristics of planar detector fabricated on CZTS grown by VGF is shown in Figure 3.8 (a). For this detector, the leakage current was observed to be 15 nA for a bias voltage of +500 V applied to one of the electrodes and for a reverse bias (–500 V) applied on the same electrode, showing a symmetric leakage current at the two bias voltages. Thus, VGF grown CZTS device showed lower leakage current (which is desirable since leakage current contributes to device noise) at even higher bias as compared

to the VBM grown CZTS device. The bulk resistivity has been calculated for the same voltage range and was found to be 2.03×10^9 Ω-cm.

Figure 3.8 (b) shows log *J*-log *V* plot representing the variation of the current density J as a function of the negative bias voltage V. The plot shows two different linear regions, fitted with a straight line. The slope of the Region I (20–200 V) is found to be unity, which suggests an Ohmic type of current flow. In higher bias region, the Region II, the slope of the fitted line was 1.68 which does not suggest a space charge limited current region but lies within the Lampert's triangle and may be related to trap SCLC (slope ≥ 1 and < 2), where defects play a role as recombination centers leading to slower rise in current with increasing bias voltage [46].

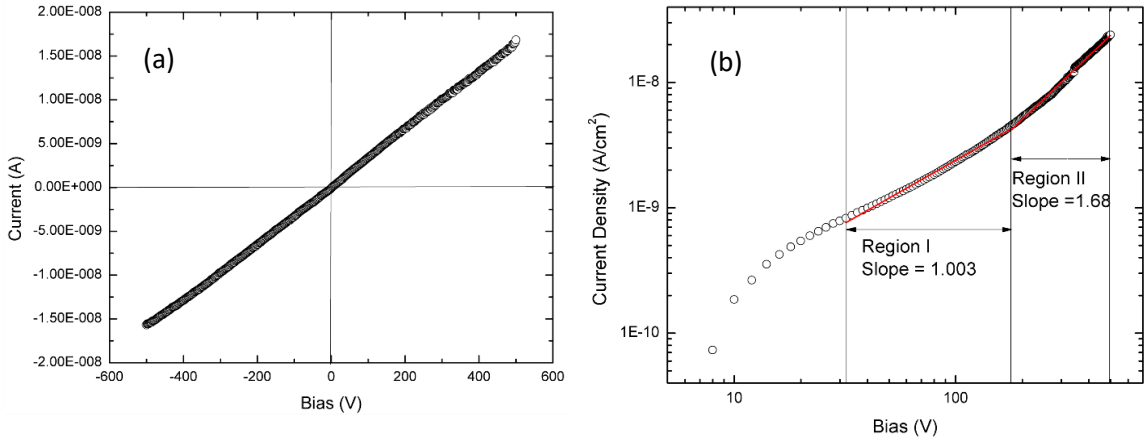

Figure 3.8 (a) Variation of leakage current as a function of bias voltage in a planar detector of CZTS grown by VGF; measured at room-temperature and under dark. (b) The negative polarity *I*-*V* characteristic has been replotted as log *J* – log *V* plot. The solid lines are the linear fits to the log *J* – log *V* curves; slopes of the linear fits are stated in the plots.

CHAPTER 4

RADIATION DETECTION

4.1 OVERVIEW

This chapter briefly describes how radiation interacts with semiconductor material such as CZTS, instrumentation associated with radiation detection measurements, and the results of radiation detection studies on fabricated VBM grown CZTS detector. Planar detectors with Au/CZTS/Au (MSM) configuration were prepared and characterized as explained in previous chapters. These well characterized detector exhibiting best electrical properties was used for radiation measurements. The analog spectrometer was used to obtain pulse height spectra (PHS) at different bias voltages while the detector was irradiated with a 0.9 μCi ^{241}Am radioactive point source emitting primarily 5486 keV alpha particles. The energy resolution of the radiation detector was calculated from the full width half maxima (FWHM) of the pulse signal generated by the incident alpha particles. Charge collection efficiency (CCE) of the CZTS detector was calculated at each bias voltage. CCE vs bias plot was used to find the mobility-lifetime product ($\mu\tau$) using the Hecht plot [48-49]. Charge transport properties such as drift mobility (μ) and lifetime (τ) are important parameters for radiation detection. Mobility provides information on how fast a charge carrier could move given an electric field and lifetime - a measure of average time spend by a charge carrier between its generation and recombination. High resolution detectors should exhibit high carrier mobility and high carrier lifetime. The higher the mobility-

lifetime product, the better is the chance of achieving high charge collection efficiency and energy resolution. A digital spectrometer was used for the drift mobility measurements. The average rise times of the pulses was measured at different bias voltages and drift velocity was calculated using a time-of flight method at different applied bias. The drift mobility was then calculated from the drift velocity vs. electric field plot.

4.2 RADIATION DETECTION INSTRUMENTATION

Interaction of radiation with semiconductor materials could occur through three processes: photoelectric absorption, Compton scattering, and electron-positron pair production. High energy gamma radiation detectors exploit primarily photoelectric absorption. Radiation (charge particles or electromagnetic wave such as gamma-ray), when interacts with semiconductor material, energizes electrons within the semiconductor atoms. The energized electrons get ejected from the atom's shell and become free electrons (negative charge) and give rise to corresponding hole (positive charge). On applying a strong electric field across the semiconductor device, the electron and hole pair gets separated and moves (drifts) to the respective contact electrodes. The amount of charge generated by the detector is proportional to the original energy of the incident photon. Detector's front-end electronics convert radiation induced charge into a voltage, which is then processed by a shaping amplifier and a multi-channel analyzer (MCA). The resulting data is called *pulse height spectra* (PHS), which depicts how many counts of radioactive photons interacted with the detector, and what energy was observed by the detector.

A schematic diagram of nuclear detection set-up used for this study is shown in Figure 4.1. Each component of this instrumentation has specific functions. First, a bias is used to create a potential difference to collect radiation induced charges. With a proper

selection of the bias polarity either the electrons or the holes are made to transit the detector thickness. For instance, a positive bias at the detector entrance window will force electrons to traverse the detector thickness. The charge sensitive pre-amplifier converts current generated by the induced charges, into voltage signal by integrating the current pulses. This is followed by the shaping amplifier has a differentiator (CR)-integrator(4RC) circuit and shapes the pre-amplifier output signal. It also reduces the noise by passing the signal through the band pass filter integrated in the shaping amplifier, thereby improving the signal to noise ratio. The signal is then passed to the multichannel analyser (MCA) which digitizes the amplifier output pulse and puts the number of pulses of similar height in the same bins or channels to obtain the histogram. This distribution of the histogram is defined as the pulse height spectra (PHS). The PHS shows peaks corresponding to the different incident energies. The width of the peak measured as full width at half maximum (FWHM) gives the resolution of the spectrometer. The further a peak is in terms of channel number in the MCA, the higher the corresponding energy.

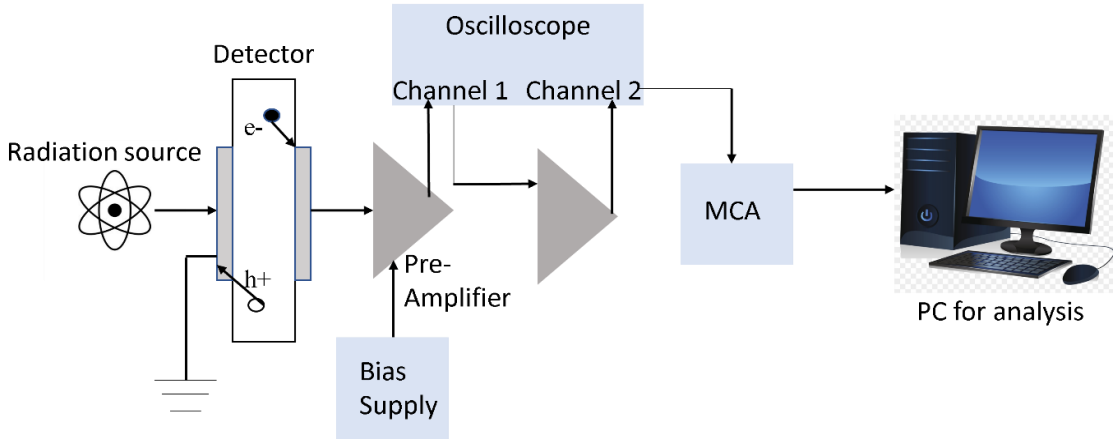

Figure 4.1 Schematic diagram of nuclear radiation detection set-up used for this study.

4.3 RADIATION DETECTION MEASUREMENTS

The analog spectrometer was used to obtain pulse height spectra at different bias voltages, which used a Cremat CR110 charge sensitive preamplifier, an Ortec 672 spectroscopy amplifier, and a Canberra Multiport II multi-channel analyzer coupled to a Genie 2000 user interface. The digital spectrometer uses the CR110 preamplifier coupled directly to a NI PCI5122 digitizer card. The digitizer card acquires the raw preamplifier pulses produced due to the alpha detector interactions. A data acquisition and analysis program have been coded in LabVIEW to control the digitizer card. The detector was illuminated by a 0.9 μCi ^{241}Am radioactive point source emitting primarily 5486 keV alpha particles. During the alpha detection measurements, the test box (Figure 4.2) was continually evacuated using a vacuum pump, to mitigate any erroneous reading caused by air current and background radiation. The radiation detectors in their vertical planar configuration produced signals when illuminated with the stated alpha source at few volts of bias. The negative polarity bias was applied at the electrode facing the source which made the electrons transit the detector width.

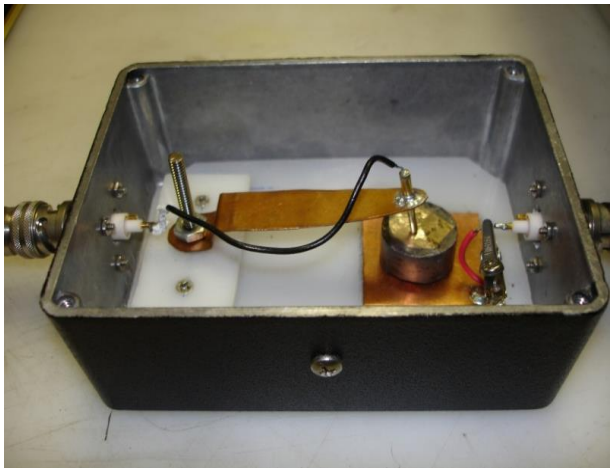

Figure 4.2 Nuclear radiation detector testing electronics box with a mounted detector.

The detector produced well-defined peaks in the pulse height spectra at voltages slightly below 50 V. Figure 4.3 shows the evolution of the alpha PHS with increasing bias. The peaks became increasingly symmetric, and their centroid position shifted steadily towards the higher energy channels, both of which indicate that the charge collection becomes more and more efficient with increasing bias. The charge collection efficiency (CCE) has been calculated at each bias voltage. CCE vs bias plots were used to find the $\mu\tau$ product using the Hecht plot [48-49]. The PHS did not show further improvement beyond a bias voltage of - 350 V at which the CCE was measured to be 97% for electrons.

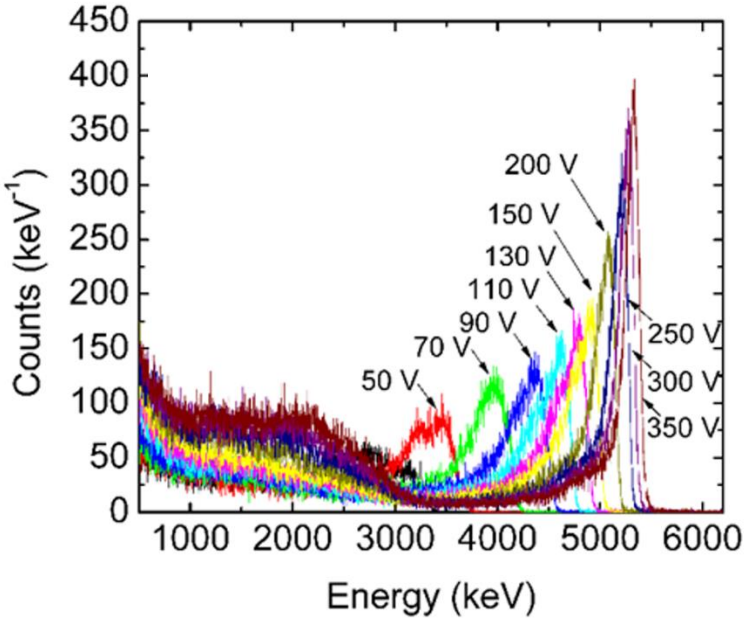

Figure 4.3 Pulse height spectra obtained at different bias voltages with VBM grown CZTS detector irradiated with an ^{241}Am radioisotope emitting primarily 5486 keV alpha particles.

With the same detector-source geometry and biasing conditions as above, charge pulses were collected at different bias voltages. The rise-time spectra were plotted at each bias. Figure 4.4 shows the variation of the rise-time spectra as a function of the bias voltage. The centroid of the rise-time peaks could be seen to shift towards the lower time

which indicates that the average duration taken by the electrons to transit the detector thickness under a given bias becomes shorter and shorter with increasing bias. This observation is commensurate with the fact that the drift velocities become higher at higher electric field. The average electron transit time was seen to saturate beyond 200 V.

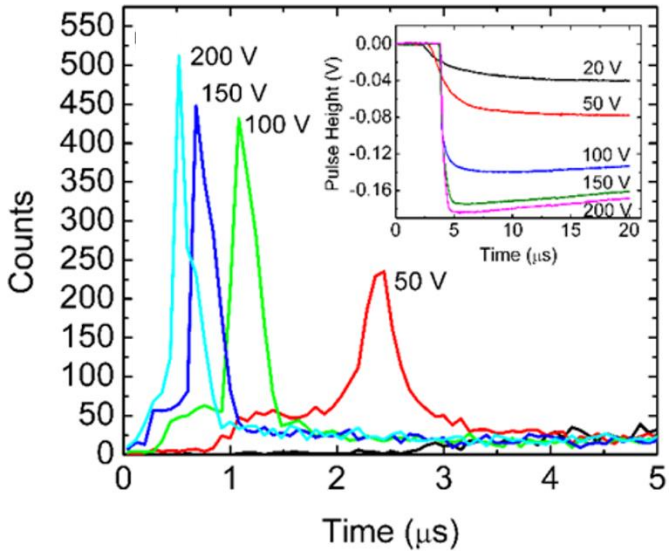

Figure 4.4 Risetime spectra obtained from preamplifier pulses under same experimental configuration. Inset shows randomly selected typical charge pulses at four different bias voltages. The increasing sharpness of the pulses indicates faster charge collection as the bias increases.

4.4 CHARGE TRANSPORT PROPERTIES

For a high-resolution semiconductor radiation detector, a prevalent figure-of-merit is the mobility-lifetime ($\mu\tau$) product of the charge carriers. The mobility-lifetime product of a detector with thickness d can be measured using Hecht's equation [48] which relates the charge collection efficiency (CCE) of a detector with the applied bias voltage V.

$$CCE = \frac{\mu\tau V}{d^2}\left[1 - \exp\left(\frac{-d^2}{\mu\tau V}\right)\right] \qquad 4.1$$

Where mobility (μ) or more specifically the drift mobility is defined as the drift velocity acquired by a charge carrier per unit electric field and carrier lifetime (τ) is the average time the charge carriers spend between its generation and recombination. The charge collection efficiency (CCE) is defined as the ratio of the amount of charge produced at the detector output to the amount of charge generated by a particular radiation-detector interaction. To determine the μτ product, PHSs are acquired as a function of bias voltages starting from as low a bias as possible. For monoenergetic alpha particle sources only one peak will be present in each PHS, as the source emits alpha particles with a single average energy of E_α (for our ^{241}Am source, it is 5486 keV). The output charge from the detector is proportional to the corresponding energy of the peak position (E_p) in the PHS for a given bias. The charge collection efficiency (CCE) is then defined as the ratio E_p/E_α and plotted as a function of the applied bias V. The CCE vs. bias plot is then fitted using a single-polarity Hecht equation (Equation 4.1) to determine the μτ product of a detector with thickness d. In this work, an absolute calibration approach was used to calibrate the spectrometer [50]. Figure 4.5 shows the variation of the charge collection efficiency of the detector as a function of the detector bias for electron transit. The μτ product for electrons was calculated to be 1.5×10^{-3} cm^2/V. The μτ product calculated using the above method is unaffected by the presence of shallow traps.

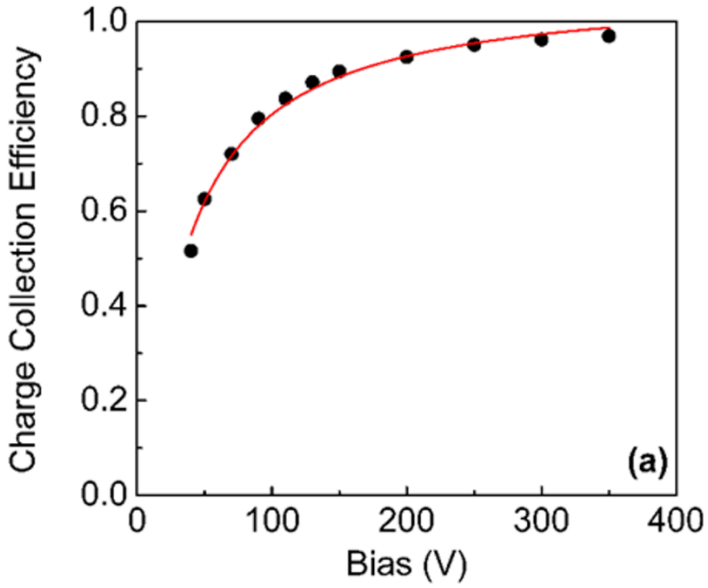

Figure 4.5 Variation of electron charge collection efficiency as a function of applied bias voltage. The solid line shows the single polarity Hecht equation fit.

A time-of-flight (TOF) method was used to calculate the drift mobility in the CZTS semiconductor. A bias V, was applied across the detector to collect the charge pairs, generated by the radiation source kept on top of the detector. The transit of the electrons and holes across the detector creates a signal at the output of the charge (current) sensitive pre-amplifier whose risetime (width) gives the transit duration (t) when plotted against time. For a linear distribution of electric field across the detector, the drift velocity v_d of the charge carriers can be calculated as d/t, where d is the thickness of the detector. A large number of pulses are recorded for a particular bias from which the average transit time is calculated. The experiment is repeated for several bias voltages after which the drift-times are plotted against the corresponding electric field (E), as

$$E = \frac{V}{d} \qquad 4.2$$

The linear plot of drift velocity (v_d) as a function of electric field (E), gives the drift mobility (μ) of the charge carrier according to the following equation:

$$v_d = \mu E \qquad 4.3$$

Figure 4.6 shows the variation of the electron drift velocities as a function of the applied electric field. The rise times for the electron pulses has been translated to the transit time t_r using a linear extrapolation method [51]. A linear fit to the plot in Figure 4.6 gives the electron drift mobility which in this case was calculated to be 710 $cm^2/V.s$ The drift mobility and the mobility-lifetime product CZTS crystals was comparable to charge transport properties reported by others [24, 47, 52].

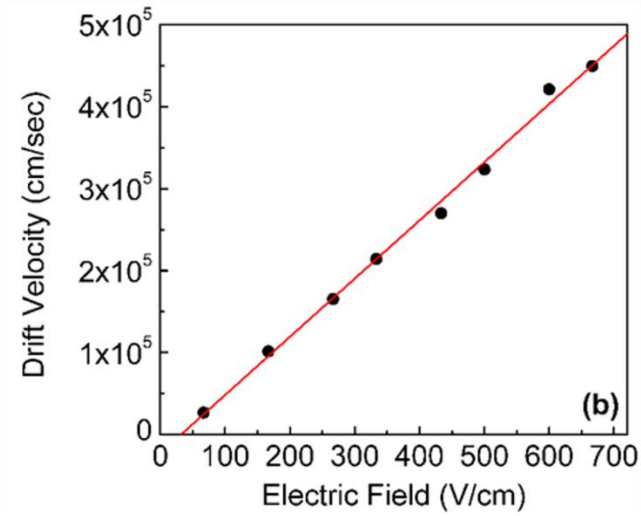

Figure 4.6 Variation of electron drift mobility in VBM grown CZTS detector as a function of applied electric field. The solid line is the linear fit to the plot.

CHAPTER 5

CONCLUSIONS

In this research thesis, growth of $Cd_{0.9}Zn_{0.1}Te_{0.97}Se_{0.03}$ (CZTS) single crystals for room temperature radiation detection has been reported. Two growth methods, modified vertical Bridgman method (VBM) and vertical gradient freeze (VGF) method, have been used to grow the CZTS crystals from in-house zone refined 7N (99.99999%) purity elemental precursors. For the vertical Bridgman method, a single pass through the three-zone heating furnace was carried out instead of the usual three passes associated with the VBM method. The goal was to reduce the growth duration without compromising crystal quality. Reduction in growth duration will decrease production cost of CZTS-based temperatures detectors. Further, growth method was modified so that growth could be conducted at a lower temperature offering reduction in temperature related stress during crystal growth, which often introduce inhomogeneity and morphological defects in growing crystal. Vertical gradient freeze (VGF) method offers further reduction in growth duration as it is inherently a faster growth method than VBM. In the VGF method, the ampoule was stationary, and the growth was carried out by the careful control of thermal gradient generated in the furnace. This method could further enhance the homogeneity of the grown crystals by mitigating the general inhomogeneity caused by the dynamic movement of the ampoule in the VBM method.

The CZTS crystals grown using both VBM and the VGF method were then processed by etching and chemo mechanical polishing (CMP), for device fabrication. The highly crystalline (~88.7% crystallinity) nature of the grown crystals was verified by performing powder x-ray diffraction (XRD) on the grown crystals, which gave sharp and well-defined diffraction peaks. XRD showed the formation of a zincblende structure with a lattice constant of ~6.45 Å for both crystals. Elemental composition and stoichiometry of the grown crystals were examined using energy-dispersive x-ray analysis (EDX). The EDX analysis confirmed the formation of the quaternary compound in its desired stoichiometry. Although the stoichiometric composition for the crystal grown using the VGF method, showed values slightly less than the expected value, which could be attributed to the inhomogeneity caused during growth process due to temperature and high cadmium vapor pressure. X-ray photoelectric spectroscopy (XPS) was carried out on the surface of the crystal wafer. The oxidation states detected and analyzed by XPS was similar to the previously analyzed oxidation states of CdZnTe compounds.

Detectors with $11\times11\times3$ mm^3 dimension were fabricated by depositing identical metal (gold) contact on the two opposite surfaces. The current-voltage characteristics showed a leakage current ranging from 15 nA (for VGF grown CZTS crystal) at 500V to 50 nA (for VBM grown CZTS crystal) at 200V. An asymmetric I-V plot for VBM grown CZTS device was observed, while a symmetric Ohmic I-V plot was observed for the VGF grown crystal. The bulk resistivity for these fabricated devices was found to be in the range of 10^9 to 10^{10} Ω-cm. The log J–log V plots revealed a trap space charge limited current mechanism at moderate bias.

The fabricated device with the highest resistivity (~10^{10} Ω-cm), which was for CZTS device that used VBM grown crystal, was used for radiation detection studies. Alpha spectroscopy for room temperature radiation detection was carried out using a 0.9 μCi ^{241}Am alpha source primarily emitting 5486 keV alpha particles. Charge transport properties based on the alpha spectroscopic studies revealed a mobility-lifetime product of 1.5×10^{-3} cm^2/V and a drift mobility value of 710 cm^2/V-s. The observed electron-transport properties agreed with the reported values for the CZT crystals current leader for the room temperature radiation detector. Therefore, we can conclude that electrical properties of CZTS crystal produced by single pass vertical Bridgman growth (low growth duration and temperature) are close to the values reported in the literature for the best CZTS crystal.

We have carried out radiation testing only with ^{241}Am alpha source. Further work is necessary to evaluate these CZTS detector using gamma radiation sources such as ^{137}Cs and evaluate energy resolution at FWHM. Study of electrically active intrinsic defect in CZTS single crystal that interfere with detector performance will be a good tool to explain differences that were observed in CZTS devices that used crystal from VBM compared to devices based on VGF grown CZTS crystal. Furthermore, the present study was limited to simple planer detector structure other detector structure such as pixilated, guard ring, or Frisch collar detector could be investigated to increase detector performance. Recently Roy et al. has reported a CZTS Frisch collar detector displaying a 0.77% energy resolution for gamma ray detection [24].

REFERENCES

[1] B. Milbrath, A. Peurrung, M. Bliss and W. Weber, "Radiation detector materials: An overview," *Journal of Materials Research*, **23**, 2561-2581 (2008).

[2] A. Owens and A. Peacock, "Compound semiconductor radiation detectors," *Nuclear Instruments and Methods in Physics Research A*, **531**, 18-37 (2004).

[3] S. E. Pfanstiel, K. J. Hofstetter and T. A. DeVol, "Comparison of four types of gamma-and X-ray detectors for environmental applications in the 10–450 keV energy range," *J. Radioanal. Nucl. Chem.*, **223**, 89-98 (1997).

[4] G. F. Knoll, *Radiation Detection and Measurement*, 3rd ed., New York: John Wiley & Sons, Inc., 2000.

[5] P. N. Luke, R. H. Pehl and F. A. Dilmanian, "A 140-element Ge detector fabricated with amorphous Ge blocking contacts," IEEE *Trans. Nucl. Sci.,* **41**, 976-978 (1994).

[6] T.E. Schlesinger, J. Toney, H. Yoon, E. Lee, B. Brunett, L. Franks and R. James, "Cadmium zinc telluride and its use as a nuclear radiation detector material," *Materials Sci. Eng.*, **32**, 103-189 (2001).

[7] K. C. Mandal, S. H. Kang, M. Choi, J. Bello, L. Zheng, H. Zhang, M. Groza, U. N. Roy, A. Burger, G. E. Jellison, D. E. Holcomb, G. W. Wright, and J. A. Williams, "Simulation, modeling, and crystal growth of $Cd_{0.9}Zn_{0.1}Te$ for nuclear spectrometers," *J. Electron. Mater*., **35**, 1251-1256 (2006).

[8] S. D. Sordo, L. Abbene, E. Caroli, A. M. Mancini, A. Zappetteni and P. Ubertini, "Progress in the Development of CdTe and CdZnTe Semiconductor Radiation Detectors for Astrophysical and Medical Applications," *Sensors,* **9**, 3491-3526 (2009).

[9] R. M. Krishna, S. K. Chaudhuri, K. J. Zavalla and K. C. Mandal, "Characterization of $Cd_{0.9}Zn_{0.1}Te$ based virtual Frisch grid detectors for high energy gamma ray detection," *Nucl. Instrum. Methods Phys. Res. A,* **701**, 208-213 (2013).

[10] A. E. Bolotnikov, K. Ackley, G. S. Camarda, C. Chercher, Y. Cui, G. De Geronimo, J. Fried, D. Hodges, A. Hossain, W. Lee, G. Mahler, M. Maritato, M. Petryk, U. Roy, C. Salwen, E. Vernon, G. Yang and R. B. James, "An array of virtual Frisch-grid CdZnTe detectors and a front-end application-specific integrated circuit for large-area position-sensitive gamma-ray cameras," Rev. Sci. Instrum., **86**, 073114-1-5 (2015).

[11] A. Brovko, O. Amzallag, A. Adelberg, L. Chernyak, P.V. Raja and A. Ruzin, "Effects of oxygen plasma treatment on CdZnTe material and devices," *Nucl. Instrum. Meth. Phys. Res. A,* **1004**, 165343-165354 (2021).

[12] G. Lioliou, S. Butera, A.B. Krysa and A.M. Barnett, “The response of thick (10 μm) AlInP x-ray and γ-ray detectors at up to 88 keV,” *J. Appl. Phys*., **129**, 243105-12 (2021).

[13] W.R. Willing, “Mercury iodide as a gamma spectrometer,’’ *Nuclear Instruments and Methods*, **96**, 615-616 (1971).

[14] F. Nava, G. Bertuccio, A. Cavallini and E. Vittone, "Silicon carbide and its use as a radiation detector material," *Measurement Science and Technology*, **19**, 102001-1-25, (2008).

[15] K.C. Mandal, S.H. Kang, M. Choi, A. Kargar, M.J. Harrison, D.S. McGregor, A.E. Bolotnikov, G.A. Carini, G.S. Camarda and R.B. James, “Characterization of Low-Defect $Cd_{0.9}Zn_{0.1}Te$ and CdTe Crystals for High-Performance Frisch Collar Detectors,” *IEEE Trans. Nucl. Sci*., **54**, 802-806 (2007).

[16] K. Iniewski, “CZT detector technology for medical imaging,” *J. of Instrumentation*, **9**, C11001-1-7 (2014).

[17] P.M. Johns and J.C. Nino, “Room temperature semiconductor detectors for nuclear security,” J. Appl. Phys., **126**, 040902-20, (2019).

[18] J. Tang, F. Kislat and H. Krawczynski, “Cadmium Zinc Telluride detectors for a next-generation hard X-ray telescope,” *Astroparticle Phys*., **128**, 102563-11 (2021).

[19] A. Zappettini, L. Marchini, M. Zha, G. Benassi, N. Zambelli, d. Calestani, L. Zanotti, E. Gombia, R. Mosca, M. Zanichelli, et al., “Growth and characterization of CZT crystals by the vertical Bridgman method for x-ray detector applications,” *IEEE Trans.Nucl. Sci.,* **58**, 2352-2356 (2011).

[20] M. Amman, J.S. Lee, P.N. Luke, H. Chen, S.A. Awadalla, R. Redden and G. Bindley, “Evaluation of THM-grown CdZnTe material for large-volume gamma-ray detector applications,” *IEEE Trans. Nucl. Sci.*, **56**, 795-799 (2009).

[21] U.N. Roy, A. Burger and R.B. James, “Growth of CdZnTe crystals by travelling heater method,” *J. Cryst. Growth*, **379**, 57-62 (2013).

[22] A.E. Bolotnikov, K. Ackley, G.S. Camarda, Y. Cui, J.F. Eger, G. De Geronimo, C. Finfrock, J. Fried, A. Hossain, W. Lee, M. Prokesch, M. Petryk, J.L. Reiber, U.N. Roy, E. Vernon, G. Yang and R.B. James, “High-efficiency CdZnTe gamma-ray detectors,” *IEEE Trans. Nucl. Sci.,* **62**, 3193-3198 (2005).

[23] U.N. Roy, G.S. Camarda, Y. Cui, R. Gul, G. Yang, J. Zazvorka, V. Dedic, J. Franc and R. James, “Evaluation of CdZnTeSe as a high-quality gamma-ray spectroscopic material with better compositional homogeneity and reduced defects,” *Sci. Rep*., **9**, 7303-7 (2019).

[24] U.N. Roy, G.S. Camarda, Y. Cui, and R.B. James, “High-resolution virtual Frisch grid gamma-ray detectors based on as-grown CdZnTeSe with reduced defects,” *Appl. Phys. Lett.*, **114**, 232107-4 (2019).

[25] J.W. Kleppinger, S.K. Chaudhuri, U.N. Roy, R.B. James and K.C. Mandal, “Growth of $Cd_{0.9}Zn_{0.1}Te_{1-y}Se_y$ single crystals for room-temperature gamma ray detection,” *IEEE Trans. Nucl. Sci*., **68**, 2429-2434 (2021).

[26] R. Nag, S. K. Chaudhuri, J.W. Kleppinger, O.F. Karadavut and K.C. Mandal, “Characterization of vertical Bridgman grown $Cd_{0.9}Zn_{0.1}Te_{0.97}Se_{0.03}$ single

crystal for room-temperature radiation detection," *J. Mater. Sci.: Mater. Electron.*, **32**, 26740-26749 (2021).

[27] U.N. Roy, G.S. Camarda, Y. Cui, R. Gul, A. Hossain, G. Yang, J. Zazvorka, V. Dedic, J. Franc and R.B. James, "Role of selenium addition to CdZnTe matrix for room-temperature radiation detector applications," *Sci. Rep.*, **9**, 1620-7 (2019).

[28] S.K. Chaudhuri, M. Sajjad; J.W. Kleppinger and K.C. Mandal, "Charge transport properties in CdZnTeSe semiconductor room-temperature γ-ray detectors," *J. Appl. Phys.*, **127**, 245706-1-8, (2020).

[29] Yakimov, D. Smith, J. Choi and S. Araujo, "Growth and characterization of detector-grade CdZnTeSe by horizontal Bridgman technique," *Proc. SPIE*. **1114**, 111141N-1-7 (2019).

[30] P. Rudolph, *Handbook of Crystal Growth*: Elsevier, 2015.

[31] M. Sajjad, J. W. Kleppinger and K. C. Mandal, "Crystal growth, characterization, and fabrication of $Cd_{0.9}Zn_{0.1}Te$ monolithic pixilated detectors for high energy gamma ray," *Proc. SPIE*, **1114**, 11141T-1-12 (2019).

[32] S. K. Chaudhuri, K. Nguyen, L. Matei, V. Buliga, M. Groza, A. Burger and K. C. Mandal, "Large Area $Cd_{0.9}Zn_{0.1}Te$ Pixelated Detector: Fabrication and Characterization," *IEEE Trans. Nucl. Sci*., **61**, 793-798 (2014).

[33] C. Oner, K.V. Nguyen, R.O. Pak, M.A. Mannan and K.C. Mandal, "Investigation of thermally evaporated high resistive B-doped amorphous selenium alloy films and metal contact studies," *SPIE Proc.*, **9593**, 95931I-1-11 (2015).

[34] W. G. Pfaan, *Zone Melting*, 2nd ed., Kreiger Publishing, 1978.

[35] M. Sajjad, *Room temperature semiconductor radiation detectors based on CdZnTe and CdZnTeSe*, University of South Carolina, 2020.

[36] M.J. Harrison, A.P. Graebner, W.J. McNeil and D.S. McGregor, "Carbon coating of fused silica ampoules," *J. Cryst. Growth*, **290**, 597-601 (2006).

[37] M. Zha, F. Bissoli, A. Zappettini, G. Zuccalli, L. Zanotti and C. Paorici, "Heat treatment in semi-closed ampoule for obtaining stoichiometrically controlled cadmium telluride," *J. Cryst. Growth*, **237-239**, 1720-1725 (2002).

[38] T. B. Wu, J. S. Chen, C. D. Chiang, Y. M. Pang and S. J. Yang, "Study on polished and etched surfaces of polar (111) CdTe by x-ray photoelectron spectroscopy and grazing incidence x-ray diffraction," *J. Appl. Phys*. **71**, 5212-5216 (1992).

[39] P. Bartolo-Pérez, M. Farías, R. Castro-Rodríguez and J. Peña, "XPS analysis of oxidation states of Te in CdTe oxide films grown by rf sputtering with an Ar-NH3 plasma," *Superficies y Vacío*, **12**, 8-11 (2001).

[40] A. A. Rouse, C. Szeles, J.-O. Ndap, S. A. Soldner, K. B. Parnham, D. J. Gaspar, M. H. Engelhard, A. S. Lea, S. V. Shutthanandan, T. S. Thevuthasan and D. R. Baer, "Interfacial Chemistry and the Performance of Bromine-Etched CdZnTe Radiation Detector Devices," *IEEE Trans Nucl Sci*, **49**, 2005-2009 (2002).

[41] J. Häring, J. G. Werthen, R. H. Bube, L. Gulbrandsen, W. Jansen and P. Luscher, "Study of cleaved, oxidized, etched, and heat treated CdTe surfaces," *J. Vac. Sci. Technol. A*, **1**, pp. 1469-1472 (1983).

[42] Y. S. Wu, C. R. Becker, A. Waag, R. Schmiedl, S. Einfeldt and G. Landwehr, "Oxygen on the (100) CdTe surface," *J. Appl. Phys*, **73**, 7385-7388 (1993).

[43] K. C. Mandal, S. Basu, and D. N. Bose, "Effect of surface modification on sub-bandgap response of n-CdTe photoelectrodes", *Surf. Sci*. **188**, 235-240 (1987).

[44] K. C. Mandal, S. Basu, and D. N. Bose, "Effects of surface modification on n-cadmium telluride photoelectrochemical solar cells", *J. Phys. Chem.* **91**, 4011-4013 (1987).

[45] N. F. Mott, and R. W. Gurney, *Electronic Processes in Ionic Crystals*, Oxford University Press, New York, (1940).

[46] M. A. Lampert, "Volume-controlled current injection in insulators", *Rep. Prog. Phys*. **27**, 329-367 (1964).

[47] S. K. Chaudhuri, M. Sajjad, J. W. Kleppinger, and K. C. Mandal, "Correlation of Space Charge Limited Current and γ-Ray Response of $Cd_xZn_{1-x}Te_{1-y}Se_y$ Room-Temperature Radiation Detectors", *IEEE Electron Device Lett*. **41**, 1336-1339 (2020).

[48] K. Hecht, "Zum Mechanismus des lichtelektrischen Primärstromes in isolierenden Kristallen", *Zeitschrift für Physik* **77**, 235-245 (1932).

[49] Z. He, G. F. Knoll, and D. K. Wehe, "Direct measurement of product of the electron mobility and mean free drift time of CdZnTe semiconductors using position sensitive single polarity charge sensing detectors", *J. Appl. Phys*. **84**, 5566-5569 (1998).

[50] T. A. M. Fiducia, B. G. Mendis, K. Li, C. R. M. Grovenor, A. H. Munshi, K. Barth, W. S. Sampath, A. Abbas, and J. W. Bowers, "Understanding the role of selenium in defect passivation for highly efficient selenium-alloyed cadmium telluride solar cells", *Nat. Energy*. **4,** 504-511 (2019).

[51] S. K. Chaudhuri, R. M. Krishna, K. J. Zavalla, L. Matei, V. Buliga, M. Groza, A. Burger, and K. C. Mandal, "$Cd_{0.9}$ $Zn_{0.1}$ Te Crystal Growth and Fabrication of Large Volume Single-Polarity Charge Sensing Gamma Detectors", *IEEE Trans. Nucl. Sci*. **60**, 2853-2858 (2013).

[52] S. K. Chaudhuri, J. W. Kleppinger, O. F. Karadavut, R. Nag, and K. C. Mandal, "Quaternary Semiconductor $Cd_{1-x}Zn_xTe_{1-y}Se_y$ for High-Resolution, Room-Temperature Gamma-Ray Detection", *Crystals* **11**, 827-22 (2021).